

POLITECNICO
MILANO 1863

SCUOLA DI INGEGNERIA INDUSTRIALE
E DELL'INFORMAZIONE

Recovery-based error estimators for 1D and 2D hyperbolic differential problems

Tesi di Laurea Magistrale in
Mathematical Engineering - Computational Science and Computational Learning

Francesco Carlo Genito, 247131

Advisor:
Prof. Annalisa Buffa
Prof. Paola Francesca Antonietti

Co-advisors:
Dr. Pablo Antolin Sanchez
Ferhat Sindy

Academic year:
2025-2026

Abstract: This work adapts recovery-based error estimation, traditionally used for static elliptic problems, to hyperbolic wave equations. The mathematical model relies on a standard Galerkin finite element method using piecewise linear or quadratic polynomials. This spatial discretization is paired with Crank-Nicolson and Newmark time-stepping schemes. We apply polynomial preserving recovery techniques to estimate spatial gradients, L^2-norms, and time derivatives, according to the natural energy norm of the problem. In the baseline case of the acoustic wave equation, the recovered quantities successfully capture both the spatial and temporal errors. They maintain the expected asymptotic convergence rates. However, extending this framework to shear electrostatic Alfvén waves highlights a structural issue. The mixed formulation artificially bounds the spatial convergence. This stability constraint inherently causes the recovery operators to fail. By switching to a decoupled scheme, we successfully bypass this stability bottleneck. This shift restores the optimal convergence order of the primary fields. It allows the a-posteriori estimators to accurately approximate the true decoupled energy norm of the system. As a final validation, we use these error indicators to control a dynamic adaptive mesh refinement strategy. The algorithm correctly localizes the moving wave fronts and refines the elements only where necessary. This demonstrates that recovery-based methods can also be extended to hyperbolic problems and be a true help in estimating and localizing the exact error.

Key-words: recovery-based error estimation, a-posteriori convergence, hyperbolic differential problems, FEM, time-discretization schemes, AMR

1. Introduction

The mathematical modeling of complex physical phenomena is highly dependent on Partial Differential Equations (PDEs). Since it is difficult to solve these equations exactly for real world applications, these equations must be approximated using numerical discretization methods. However, translating a continuous differential model into a discrete one cannot actually capture the full set of its information. Instead, an approximation error is introduced and it must be rigorously quantified in order to assess the effectiveness of the numerical method.
Traditionally, the reliability of a numerical scheme is established by using *a priori* error estimates. Although these estimators are fundamental for proving the theoretical asymptotic rates of a method, they only consist of upper global bounds depending on the exact solution. Consequently, *a priori* bounds cannot tell us where the error is localized within the computational domain. To overcome this limitation, *a posteriori* error estimation can be employed. Since they rely only on the computed discrete solution and the known problem data, *a posteriori* estimators yield a quantitative, computable evaluation of the error.
For the Finite Element Method (FEM) [5], the theory and practice of *a posteriori* error indicators is well established. For instance, some comprehensive reviews, such as those of Ainsworth and Oden [2] or Grätsch and Bathe [16], highlight how these tools can be used to evaluate the accuracy of the numerical solution. Indeed, by collecting local information

about the error distribution, these estimators allow us to identify regions of poor approximation within the domain, providing the tools to drive adaptive mesh refinement strategies.
Within this established FEM literature, *a posteriori* error estimation is generally divided into two main paradigms: residual-based and recovery-based methods. Residual-based estimators are based on the idea that the underlying PDE produces a residual. The numerical error is bounded from above and below by the dual norm of the residual up to a constant [7]. Although widely used, this approach has a major practical drawback: estimators are equation-dependent. Deriving and implementing them for complex or coupled multi-physics systems can be nontrivial and repetitive, as the entire estimator must be reformulated whenever the equations change.
To overcome this issue, the recovery-based approach represents an equation-independent alternative. The core philosophy of this methodology, originally pioneered by Zienkiewicz and Zhu [31], is to post-process the gradient of the numerical finite element solution. Rather than relying on the PDE residual, these methods apply a local recovery operator, which constructs a more accurate and superconvergent approximation of the true continuous gradient field, by means of the actual numerical solution. The local error is then estimated simply by evaluating the difference between the recovered and numerical gradient. A fundamental finding within this framework is the Polynomial Preserving Recovery (PPR), introduced by Zhang and Naga [29]. This technique recovers the gradient by fitting a higher-degree polynomial to the nodal solution and differentiating it. Compared to earlier patch recovery techniques, PPR aims to reach superconvergence across different mesh topologies and can be seamlessly extended to higher order finite element spaces. While this specific PPR technique has proven to be a highly solid tool for assessing spatial numerical errors in stationary problems, extending these recovery principles to space-time dynamics shows new challenges.
The transition to a space-time setting is particularly demanding for hyperbolic partial differential equations, such as the standard acoustic wave equation and, more specifically, the Alfvén wave equations governing plasma physics. In these systems, accurately capturing the propagation of waves over time requires rigorous error control in both the spatial and temporal discretizations. While *a posteriori* error estimation for wave equations has obtained more attention nowadays, the majority of existing finite element approaches depend heavily on residual evaluations or elliptic reconstructions. For instance, early applications of recovery techniques to hyperbolic problems, such as the work by Picasso [20], successfully utilized Zienkiewicz-Zhu gradient recovery to derive an anisotropic error estimator for the wave equation. However, this formulation relies on an elliptic reconstruction that exclusively evaluates the spatial discretization error, entirely neglecting the temporal error contribution. Additional developments attempted to capture the full space-time error, such as the combined estimator developed by Gorynina, Lozinski, and Picasso [14]; nevertheless, their methodology remains strictly residual-based, requiring the equation-dependent evaluation of the continuous mathematical residual at each time step. Considering the computational bottlenecks of residual-based methods, very recent work by Sindy, Buffa, and Picasso [25] introduced a highly innovative space-time recovery indicator. Yet, this approach was designed specifically to post-process point values from high-order Finite Difference Methods (FDM), interpolating them into a polynomial space rather than operating natively within a full finite element formulation. Consequently, a fully equation-agnostic and recovery-based-space-time error estimator applied directly to the Finite Element Method for hyperbolic problems remains absent from the available mathematical literature.
The main objective of this work is to address this methodological gap by developing a unified recovery-based error estimator for hyperbolic problems, with a specific latter focus on the Alfvén wave equations relevant to plasma physics. As a foundational step, the spatial Polynomial Preserving Recovery is extended to assess the finite element discretization of one- and two-dimensional problems wave propagation, as a temporal recovered gradient is conceptualized and implemented. Unlike the spatial domain, which relies on a formal finite element basis, the temporal evolution in this work is integrated using classical time-stepping schemes, such as the Crank-Nicolson method. Despite the absence of a continuous Galerkin formulation in time, we demonstrate that the fundamental philosophy of gradient recovery can still be applied. By aggregating the discrete solution values across consecutive time steps to construct local temporal patches, we can perform a polynomial fitting along the time axis. Differentiating this localized, time-continuous reconstruction yields a superconvergent time derivative. By comparing the recovered derivative against the standard discrete difference quotient, we obtain an *a posteriori* error indicator capable of dynamically evaluating the quality of both the spatial grid and the temporal step size.
The thesis is organized as follows: in Section 2, the general setting of Finite Element Method is described and applied to the Acoustic Wave Equation; in Section 3, the recovery-based operator is introduced and its mathematical characteristics analyzed. Moreover, we prove its superconvergence behavior under appropriate mesh and regularity assumptions. In Section 4, numerical results of the recovery-based error indicators in space and time for the 1D and 2D wave equation are analyzed and presented; in Section 5, the Alfvén wave equations are discretized and numerical experiments are performed to verify the theoretical expectations of the *a posteriori* error estimators in the context of plasma physics. Lastly, Section 6 contains conclusions and comments related to the numerical results and how they relate to the theoretical aspects.

2. The Wave Equation and its Discretization

This chapter sets out the mathematical framework to discretize the one- and two-dimensional acoustic wave equations. We discretise in space using the Galerkin Finite Element Method. Following the spatial discretization, we outline the temporal integration of the resulting semi-discrete system using the implicit Crank-Nicolson scheme.

2.1. Continuous Formulation of the Wave Equation

We introduce a continuous formulation of the acoustic wave equation in a general framework. Let $\Omega \subset \mathbb{R}^d$ (with $d \in \{1, 2\}$, since our analysis is strictly focused on 1D and 2D problems) be a bounded open domain, and let $T > 0$ represent the final time. The strong formulation of the model problem reads (see, e.g., Cohen [9]):

$$\begin{cases} \eta(\mathbf{x}) \frac{\partial^2 u}{\partial t^2}(\mathbf{x}, t) - \nabla \cdot (\gamma(\mathbf{x}) \nabla u(\mathbf{x}, t)) = f(\mathbf{x}, t) & \text{in } \Omega \times (0, T], \\ u(\mathbf{x}, t) = 0 & \text{on } \partial\Omega \times (0, T], \\ u(\mathbf{x}, 0) = u_0(\mathbf{x}) & \text{in } \Omega, \\ \frac{\partial u}{\partial t}(\mathbf{x}, 0) = v_0(\mathbf{x}) & \text{in } \Omega, \end{cases} \tag{1}$$

where $u(\mathbf{x}, t)$ denotes the wave displacement at a specific spatial point $\mathbf{x} \in \Omega$ and time $t \in (0, T]$. The functions u_0 and v_0 represent the initial displacement and velocity fields, respectively. The coefficients $\eta(\mathbf{x})$ and $\gamma(\mathbf{x})$ are strictly positive, spatially dependent functions that dictate the local wave propagation speed, defined as $c(\mathbf{x}) = \sqrt{\gamma(\mathbf{x})/\eta(\mathbf{x})}$.
To derive the weak formulation, we introduce the standard Sobolev space $V = H_0^1(\Omega) = \{v \in H^1(\Omega) \mid v|_{\partial\Omega} = 0\}$ to enforce the homogeneous Dirichlet boundary conditions. We multiply the governing equation by a test function $v \in V$ and integrate over the spatial domain Ω. Applying Green's First Identity (the multidimensional analogue of integration by parts) to the diffusive term, the boundary integral vanishes, yielding the continuous variational problem:
Find $u(\cdot, t) \in V$, $t \in]0, T[$, such that:

$$\begin{cases} \frac{d^2}{dt^2} \int_\Omega \eta(\mathbf{x}) u(\mathbf{x}, t) v(\mathbf{x})\, d\mathbf{x} + \int_\Omega \gamma(\mathbf{x}) \nabla u(\mathbf{x}, t) \cdot \nabla v(\mathbf{x})\, d\mathbf{x} = \int_\Omega f(\mathbf{x}, t) v(\mathbf{x})\, d\mathbf{x} \quad \forall v \in V, \\ u(\mathbf{x}, 0) = u_0(\mathbf{x}), \quad \frac{\partial u}{\partial t}(\mathbf{x}, 0) = v_0(\mathbf{x}) \quad \text{in } \Omega. \end{cases} \tag{2}$$

According to classical PDE theory and variational formulations (see, e.g., Raviart and Thomas [22] or Duvaut and Lions [11]), provided that the initial data satisfy $u_0 \in H_0^1(\Omega)$ and $v_0 \in L^2(\Omega)$, the variational problem (2) is well-posed. It admits a unique weak solution $u \in C^0([0, T]; H_0^1(\Omega)) \cap C^1([0, T]; L^2(\Omega))$, mathematically guaranteeing that both the displacement and velocity remain continuously bounded in time within their respective norms.

2.2. Spatial Discretization: The Galerkin Finite Element Method

To compute a numerical approximation of the continuous problem, we apply the Galerkin Finite Element Method. We focus here on the two-dimensional setting. First, we discretize the spatial domain Ω using a conforming regular partition $\mathcal{Q}_h$ comprised of non-overlapping quadrilateral elements K. Specifically, if the domain is a rectangle such that $\Omega = [0, L_x] \times [0, L_y]$, with $L_x, L_y > 0$ being the x-length and y-length of the domain, we naturally subdivide it into rectangular elements $K_{ij} = [x_{i-1}, x_i] \times [y_{j-1}, y_j], \forall i = 1, ..., N_x + 1, \forall j = 1, ..., N_y + 1$, with $N_x + 1, N_y + 1$ being the number of spatial subintervals on each axis, characterized by the local mesh sizes $h_x = \frac{L_x}{N_x+1}$ and $h_y = \frac{L_y}{N_y+1}$. We also define $h = \max\{h_x, h_y\}$, so that in our numerical test cases done on a 2D square, we will have $h = h_x = h_y$.
We then introduce the finite-dimensional discrete subspace $V_h^r \subset V$. For a generic polynomial degree $r \geq 1$, we define V_h^r as the space of globally continuous functions which are piecewise polynomials of degree r (denoted as $\mathbb{Q}_r$) on each quadrilateral element:

$$V_h^r = \left\{ v_h \in C^0(\bar{\Omega}) \mid v_h|_K \circ F_K \in \mathbb{Q}_r(\hat{K}) \quad \forall K \in \mathcal{Q}_h,\ v_h|_{\partial\Omega} = 0 \right\}, \tag{3}$$

where $\hat{K} = [-1, 1]^2$ is the standard reference square element, and $F_K : \hat{K} \to K$ is the affine mapping from the reference element to the physical element.
Let N_{dof} denote the dimension of V_h^r, and let $\{\varphi_i(\mathbf{x})\}_{i=1}^{N_{dof}}$ be the associated global Lagrangian nodal basis functions. The semi-discrete Galerkin approximation seeks a solution $u_h(\cdot, t) \in V_h^r$, expressed as a linear combination of the spatial basis functions with time-dependent scalar coefficients $U_j(t)$:

$$u_h(\mathbf{x}, t) = \sum_{j=1}^{N_{dof}} U_j(t) \varphi_j(\mathbf{x}). \tag{4}$$

Substituting this expansion into the weak formulation (2) and testing against every basis function $v_h = \varphi_i$, we obtain a coupled system of second-order ordinary differential equations (ODEs) in time:

$$M\ddot{\mathbf{U}}(t) + K\mathbf{U}(t) = \mathbf{F}(t), \tag{5}$$

where $\mathbf{U}(t) = [U_1(t), \ldots, U_{N_{dof}}(t)]^T$ is the vector of unknown nodal degrees of freedom. The global mass matrix $M \in \mathbb{R}^{N_{dof} \times N_{dof}}$, the stiffness matrix $K \in \mathbb{R}^{N_{dof} \times N_{dof}}$, and the load vector $\mathbf{F}(t) \in \mathbb{R}^{N_{dof}}$ are assembled from their local element-wise contributions, defined continuously as:

$$M_{ij} = \int_\Omega \eta(\mathbf{x}) \varphi_i(\mathbf{x}) \varphi_j(\mathbf{x})\, d\mathbf{x}, \quad K_{ij} = \int_\Omega \gamma(\mathbf{x}) \nabla \varphi_i(\mathbf{x}) \cdot \nabla \varphi_j(\mathbf{x})\, d\mathbf{x}, \tag{6}$$

$$F_i(t) = \int_\Omega f(\mathbf{x}, t) \varphi_i(\mathbf{x})\, d\mathbf{x}. \tag{7}$$

Because the basis functions $\varphi_i(\mathbf{x})$ have strictly local support and the mass and bilinear forms associated to the weak formulation (2) are symmetric and coercive, the resulting matrices M and K are highly sparse, symmetric, and positive-definite. The numerical evaluation of these integrals is performed on the reference element $\hat{K}$ using standard Gauss-Legendre quadrature rules to assure exact integration of the polynomial terms.

2.3. Temporal Discretization: The Crank-Nicolson Scheme

Having reduced the continuous partial differential equation to the semi-discrete system of ordinary differential equations (5), the final step consists of integrating this system in time. To do so, we introduce a uniform partition of the time interval $(0, T]$. Let $\Delta t > 0$ be the time step size, defining a set of discrete time instants $t^n = n\Delta t$ for $n = 0, 1, \ldots, N_t$, where $N_t = T/\Delta t$.
Rather than applying a direct time-stepping method to the second-order ODE, it is standard practice to rewrite the equations into a mathematically equivalent system of two coupled first-order ODEs. This is achieved by introducing the auxiliary nodal velocity vector $\mathbf{V}(t) = \dot{\mathbf{U}}(t)$. The semi-discrete system then takes the form:

$$\begin{cases} \dot{\mathbf{U}}(t) = \mathbf{V}(t), \\ M\dot{\mathbf{V}}(t) = \mathbf{F}(t) - K\mathbf{U}(t). \end{cases} \tag{8}$$

To advance this system from t^n to t^{n+1}, we apply the Crank-Nicolson scheme. Let $\mathbf{U}^n \approx \mathbf{U}(t^n)$ and $\mathbf{V}^n \approx \mathbf{V}(t^n)$ denote the fully discrete approximations. The Crank-Nicolson method evaluates the temporal derivatives using central finite differences centered at the half-step $t^{n+1/2}$, while the state variables on the right-hand side are approximated as the arithmetic mean of their values at t^n and t^{n+1}:

$$\begin{cases} \frac{\mathbf{U}^{n+1}-\mathbf{U}^n}{\Delta t} = \frac{1}{2}\left(\mathbf{V}^n + \mathbf{V}^{n+1}\right), \\ M\left(\frac{\mathbf{V}^{n+1}-\mathbf{V}^n}{\Delta t}\right) = \frac{1}{2}\left(\mathbf{F}^{n+1} + \mathbf{F}^n\right) - \frac{1}{2}K\left(\mathbf{U}^{n+1} + \mathbf{U}^n\right). \end{cases} \tag{9}$$

To solve this coupled system efficiently at each time iteration, we can algebraically decouple the variables. By isolating $\mathbf{U}^{n+1}$ from the first equation, we obtain the explicit displacement update rule:

$$\mathbf{U}^{n+1} = \mathbf{U}^n + \frac{\Delta t}{2}\left(\mathbf{V}^n + \mathbf{V}^{n+1}\right). \tag{10}$$

Substituting (10) into the second equation of (9) and gathering all the unknown terms evaluated at t^{n+1} on the left-hand side, we derive the final linear algebraic system to be inverted at each time step:

$$\left(M + \frac{\Delta t^2}{4}K\right)\mathbf{V}^{n+1} = \left(M - \frac{\Delta t^2}{4}K\right)\mathbf{V}^n - \Delta t K\mathbf{U}^n + \frac{\Delta t}{2}\left(\mathbf{F}^{n+1} + \mathbf{F}^n\right). \tag{11}$$

Thus, the computational procedure naturally unfolds in two sequential stages: first, solving the global linear system (11) to find the new velocities $\mathbf{V}^{n+1}$, and subsequently updating the displacements $\mathbf{U}^{n+1}$ via (10).
It is crucial to emphasize the reasoning behind selecting the Crank-Nicolson scheme over explicit temporal integration methods, such as the widely used Leapfrog scheme. In the numerical simulation of hyperbolic problems, explicit methods are strictly bound by the Courant-Friedrichs-Lewy (CFL) stability condition. The CFL condition dictates that the numerical domain of dependence must encompass the physical domain of dependence; mathematically, this enforces a strict upper bound on the time step, requiring $c_{max}\Delta t \leq h$, where $c_{max} = \max_{x\in\Omega}\sqrt{\frac{\gamma(\mathbf{x})}{\eta(\mathbf{x})}}$. Consequently, explicit schemes force the temporal discretization step Δt to be strictly smaller than the spatial grid size h multiplied by the maximum wave speed.
However, the Crank-Nicolson method is an implicitly A-stable scheme, meaning it is unconditionally stable regardless of the chosen time step size. While this requires the potentially expensive inversion of a coupled matrix system at each iteration, it completely bypasses the restrictive CFL condition.
In the specific context of this thesis, this theoretical freedom is an absolute necessity. By removing the CFL constraint, we are permitted to deliberately set the temporal step size equal to the spatial mesh size (i.e., $\Delta t \approx h$). This particular choice guarantees that the numerical dispersion errors originating from the spatial mesh and the temporal grid are properly balanced. Ultimately, this symmetric configuration is fundamental to our analysis: it ensures that neither the spatial nor the temporal discretization error artificially dominates the other, providing an equal and fair mathematical approach to evaluate the performance of both the spatial and temporal recovery-based error estimators introduced in the following chapters.

3. The Space and Time Recovery-based Error Indicator

This chapter explores the mathematical construction and theoretical properties of spatial and temporal recovery-based error estimators. Because discretizing a continuous model inevitably introduces error, we require computable a posteriori indicators, relying strictly on discrete solutions and known data, to estimate the true discretization error in the natural energy norm, as a priori bounds cannot localize this error. We first establish the general a posteriori framework and detail polynomial preserving recovery operators for spatial finite element approximations, alongside an L^2-norm recovery

strategy for the discrete solution. Because our hyperbolic framework relies on time-stepping schemes (such as Crank-Nicolson), the numerical temporal derivative intrinsically acts as a piecewise constant field. To correct this, we introduce a dedicated temporal recovery operator to filter this noise and restore higher-order continuity in time. Finally, we formalize the superconvergence properties necessary to guarantee the asymptotic exactness of these estimators, justifying their construction and the subsequent numerical experiments.

3.1. A-Priori and A-Posteriori Error Bounds

In this section we quantify the error between the exact solution u of the continuous differential problem (1) and its numerical approximation u_h. There are two main ways to perform this error analysis: *a-priori* and *a-posteriori*. *A-priori* estimates of the error are known before the numerical solution is computed. They depend on the theoretical properties of the PDE, the regularity of the exact solution u, and the discretization parameters (e.g. the mesh size h). Before examining the *a priori* error analysis for hyperbolic differential problems, it is instructive to recall the classical convergence behavior of the Finite Element Method applied to linear elliptic problems discretized with polynomials of degree $r \geq 1$. As comprehensively detailed in [8] and [1], under appropriate regularity assumptions on the exact solution, *a priori* analysis establishes two fundamental convergence bounds. Specifically, the error measured in the natural energy norm of the problem (which is the H^1-seminorm) converges at the optimal rate of $\mathcal{O}(h^r)$. Furthermore, the error bound in the L^2-norm, typically recovered via the Aubin-Nitsche duality argument under standard dual regularity, yields an enhanced convergence rate of $\mathcal{O}(h^{r+1})$. These classical results highlight how the convergence rates scale with the polynomial degree, providing a baseline framework before shifting our focus to time-dependent problems. In a more complicated case like the acoustic wave equation (1), which is also time-dependent, the energy-norm is defined for every time instant $t \in [0, T]$ as:

$$\|u(\cdot,t)\|_E^2 = \int_\Omega \left(\frac{\partial u}{\partial t}(x,t)\right)^2 dx + \int_\Omega |\nabla u(x,t)|^2 dx = \left\|\frac{\partial u}{\partial t}(\cdot,t)\right\|_{L^2(\Omega)}^2 + |u(\cdot,t)|_{H^1(\Omega)}^2 \tag{12}$$

Generally, the natural energy-norm corresponds to the energy norm (12) evaluated at the final time $t = T$. As one can notice, a time-dependent term has appeared, hence it is important to be able to track the error across space and time norms. Several results regarding the a-priori estimates for hyperbolic differential problems have been proved, either using the Finite Element Method both in space and time (as in Baker, 1976 [4]), or using time-stepping methods such as Newmark or Leapfrog schemes after a spatial FEM discretization (as in Chapter 14.5 of Quarteroni, Valli, 1994 [21]). Both the strategies led to the following result:

Theorem 3.1 (A Priori Error Estimates for the Fully Discrete Wave Equation)**.** *Let u be the exact weak solution to the continuous acoustic wave equation (2). Let $u_h^n \in V_h^r$ denote its fully discrete Galerkin finite element approximation at time $t^n = n\Delta t$, computed on a shape-regular mesh $\mathcal{Q}_h$ with characteristic size h. The temporal integration is performed using an unconditionally stable, second-order Newmark scheme (specifically, with parameters $\gamma = \frac{1}{2}$ and $\beta \geq \frac{1}{4}$, corresponding to the implicit Crank-Nicolson or average acceleration method).*
Assuming the exact solution exhibits sufficient space-time regularity, such that $u \in C^2([0,T]; H^{r+1}(\Omega)) \cap C^3([0,T]; H^1(\Omega)) \cap C^4([0,T]; L^2(\Omega))$, there exists a generic constant $C > 0$, dependent on the continuous solution and the physical parameters but strictly independent of h and Δt, such that the maximum error in the spatial energy norm over the discrete time steps satisfies:

$$\max_{0 \leq n \leq N_t} |u(t^n) - u_h^n|_{H^1(\Omega)} \leq C\left(h^r + \Delta t^2\right). \tag{13}$$

Furthermore, the corresponding optimal error bound in the L^2 norm is given by:

$$\max_{0 \leq n \leq N_t} \|u(t^n) - u_h^n\|_{L^2(\Omega)} \leq C\left(h^{r+1} + \Delta t^2\right). \tag{14}$$

Theorem 3.1 is powerful to get an idea of the asymptotic convergence rate of the error (i.e., how fast the numerical solution u_h converges, as the mesh size h and/or the timestep Δt are refined, to the true solution u), but these *a-priori* estimators have some drawbacks which motivate the necessity of switching to an *a-posteriori* logic: first of all, these estimators can be computed only by knowing the exact solution u, which is not available analytically in differential problems; furthermore, it is also difficult to compute the right-hand-side terms in the inequalities (13, 14), due to the multiplicative constant C being unknown.
In order to have a computable estimate, which uses only the numerical solution u_h, *a-posteriori* error estimator's theory has been developed. The idea relies on constructing an error indicator that relies only on u_h and the known problem data (such as coefficients and source terms), and it is used to assess the quality of the approximation in local terms, as this quantity can be computed locally for each element/interval coming from the discretization. This strategy of locally estimating the error allows also for adaptive mesh refinement strategies, which can be useful to reduce the error in a specific area where it is more concentrated (e.g. steeper gradients, boundaries, etc.).
The standard way to define an a-posteriori computable error estimate is by finding a function $\eta : V_h^r \to \mathbb{R}$, which takes as input the numerical solution u_h and returns a potential error indicator which approximates the exact error, measured in the natural energy norm associated with the specific differential problem:

$$\|u - u_h\|_E \approx \eta(u_h)$$

In order to assess the *a-posteriori* error indicator, two fundamental properties must be defined: *reliability* and *efficiency*. An estimator is considered reliable if it constitutes a guaranteed upper bound for the true error, up to a global constant $C_{rel} > 0$ and higher-order terms (h.o.t.):

$$\|u - u_h\|_E \leq C_{rel}\eta(u_h) + \text{h.o.t.} \tag{15}$$

Reliability is essential to ensure that the actual error is systematically controlled. On the other hand, the estimator must also be efficient, providing a lower bound to the true error to prevent severe overestimations and unnecessary mesh refinement:

$$\eta(u_h) \leq C_{eff}\|u - u_h\|_E + \text{h.o.t.} \tag{16}$$

To quantify the sharpness of these bounds in practical computations, it is standard practice to introduce the *effectivity index*, defined simply as the ratio of the estimated error to the exact error:

$$I_{eff} = \frac{\eta(u_h)}{\|u - u_h\|_E}. \tag{17}$$

Furthermore, an *a-posteriori* estimator is said to be *asymptotically exact* when the effectivity index approaches unity as the discretization parameter vanishes (i.e., $\lim_{h\to 0} I_{eff} = 1$).

3.2. The Recovery-Based Approach for Elliptic Problems: Introduction to the Spatial Gradient

The recovery-based error estimation approach is a widely used technique in Finite Element Analysis for constructing *a-posteriori* error estimators. In this chapter, the main idea presented by Naga and Zhang in their famous study [29] is described. It will then be related to the typical energy norm of the discretization error of a hyperbolic differential problem solved with Finite Element Method and Crank-Nicolson as described in Chapter 2. This norm, as defined in (12), corresponds to the sum of the L^2-norm of the temporal derivative and the H^1-seminorm of the difference between the exact solution u and the numerical solution u_h, namely:

$$\|u - u_h\|_E^2(T) = \int_\Omega \left(\frac{\partial u}{\partial t}(x,T) - \frac{\partial u_h}{\partial t}(x,T)\right)^2 dx + \int_\Omega |\nabla u(x,T) - \nabla u_h(x,T)|^2 dx \tag{18}$$

Specifically, in this section, we will focus on the estimation of the spatial gradient of the error; in the next section, an indicator for the temporal derivative will be conceptualized.
The key intuition behind Zhang and Naga's work is to recover a more accurate approximation of the true gradient ∇u by applying a specific postprocessing operator $G_h : V_h^r \to V_h^r$ to the discrete Finite Element solution $u_h \in V_h^r$, such that the "recovered" gradient $G_h u_h$ approximates the exact gradient ∇u with higher accuracy than how the discrete gradient ∇u_h does (known as *superconvergence* property). This leads to the following definition of the error indicator:

$$\eta_x(u_h) = \left(\sum_{K\in\mathcal{Q}_h} \|G_h u_h - \nabla u_h\|_{L^2(K)}^2\right)^{1/2} \tag{19}$$

The error indicator (19) is directly computable by knowing only the numerical solution u_h on each element $K \in \mathcal{Q}_h$, where $\mathcal{Q}_h$ is the quadrilateral mesh as defined in Chapter 2. The main result expected from this approach is that, as the mesh size h is refined, the *a-posteriori* error indicator (19) converges to the true spatial error, i.e.:

$$\eta_x(u_h) \xrightarrow{h\to 0} \|\nabla u - \nabla u_h\|_{L^2(\Omega)} \tag{20}$$

In the next subsections, a precise mathematical description of the recovery operator and its properties is given, in order to then derive the superconvergence property and prove the effectivity and reliability of the error estimator (19).

3.3. Mathematical Derivation of the Post-Processing Operator G_h for Linear FEM

We start by considering a one-dimensional domain, i.e. $\Omega = [a, b] \subset \mathbb{R}$, which is discretized in $N_x + 2$ equispaced nodes $x_i = a + ih, i = 0, ..., N_x + 1$ with mesh size $h = \frac{b-a}{N_x+1}$. Here, the general setting of the Finite Element is considered as in Chapter 2, supposing to work with piecewise linear polynomials for simplicity, hence $r = 1$. Since the spatial error is taken into consideration, we neglect the time dependency for this section, and consider a generic time instant $t^n, n \in \{0, 1, ..., N_t\}$, and evaluate the problem at that specific time.
Let $V_h^1 \subset H^1(\Omega)$ be the Finite Element space of degree 1, with basis functions $\{\varphi_i(x)\}_{i=0}^{N_x+1}$, and let $u_h \in V_h^1$ be the numerical solution of the model problem defined in Chapter 2. Following the Polynomial Preserving Recovery (PPR) strategy [19], the recovery operator is defined as a map $G_h : V_h^1 \to V_h^1$, such that $G_h u_h \in V_h^1$, which allows it to gain one degree higher than the numerical gradient ∇u_h, which instead is piecewise constant locally on each subinterval. Since the purpose is to increase the degree of the recovered gradient by one with respect to the numerical one, $G_h u_h$ is defined at each node $x_i \in \Omega$ as the analytical derivative of a local polynomial p_{x_i} of degree 2 (one order higher than the degree of polynomials imposed in the subspace V_h^1). The local polynomial $p_{x_i} \in \mathbb{P}^2(K_{x_i})$ is created by an exact polynomial fit through the nodal values of the numerical solution u_h in a neighborhood of the node x_i. More specifically, for each

internal node $x_i, i = 1, ..., N_x$, a three-point local stencil $K_{x_i} = \{x_{i-1}, x_i, x_{i+1}\}$ is defined to exactly interpolate a local quadratic polynomial $p_{x_i} \in \mathbb{P}^2(K_{x_i})$ through the nodal values of the numerical solution u_h at the stencil nodes, namely $u_h(x_{i-1}), u_h(x_i), u_h(x_{i+1})$. For the external nodes x_0, x_{N_x+1}, we consider respectively an all-left and an all-right stencils, i.e. $K_{x_0} = \{x_0, x_1, x_2\}$ and $K_{N_x+1} = \{x_{N_x-1}, x_{N_x}, x_{N_x+1}\}$, together with the numerical solution evaluated at the 3 nodes of these stencils. After fitting the local polynomial p_{x_i} for each node, the recovery-based error estimator is defined in the Finite Element space V_h^1:

$$G_h u_h(x) = \sum_{i=0}^{N_x+1} G_h u_h(x_i)\varphi_i(x)$$

where each coefficient $G_h u_h(x_i)$ is defined as the analytical first-order derivative of the local quadratic polynomial p_{x_i} evaluated at $x = x_i$, i.e.:

$$G_h u_h(x_i) = \left.\frac{dp_{x_i}(x)}{dx}\right|_{x=x_i}$$

In this way, it is guaranteed that the coefficients of the expansion of $G_h u_h$ correspond to a correct reconstruction of the spatial gradient from the numerical solution u_h. The plot shown in Figure 1 clarifies how the exact gradient ∇u (black

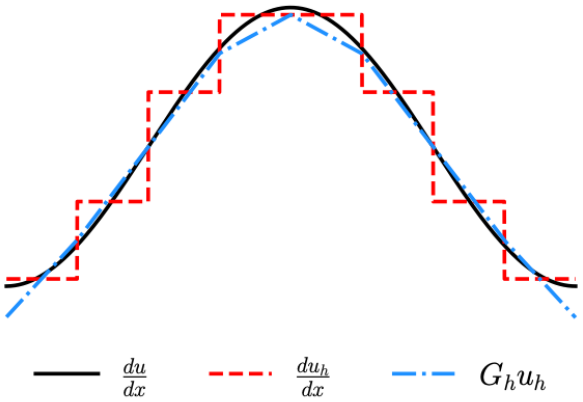

Figure 1: Comparison between Exact, Numerical and Recovered Spatial Gradient in 1D

line), the numerical gradient ∇u_h (red line), and the recovered gradient $G_h u_h$ (blue line) compare in a 1D setting. The graph clearly shows that the recovered gradient, being piecewise linear, approximates better the behavior of the exact one, rather than how the piecewise constant numerical gradient does.

When switching to a 2D setting, the procedure of exact interpolation will become less straightforward due to the geometry of the nodes. Assume for simplicity a quadrilateral mesh $\mathcal{Q}_h$ as defined in Section 2, but the reasoning can be extended also to other shape-regular meshes. In this case, the exact gradient of the solution of (1) will be two-dimensional, i.e. $\nabla u(x, y) = \left(\frac{\partial u}{\partial x}, \frac{\partial u}{\partial y}\right)(x, y)$. Therefore, in order to adapt the definition of the post-processing operator for the two-dimensional case, and sticking to the Finite Element setting with piecewise linear polynomials, we get $G_h : V_h^1 \to V_h^1 \times V_h^1$, such that:

$$G_h u_h(x, y) = \sum_{i=0}^{N_x+1} \sum_{j=0}^{N_y+1} G_h u_h(x_i, y_j)\varphi_{i,j}(x, y) \tag{21}$$

with $\{\varphi_{i,j}(x, y)\}_{i,j=0}^{N_{dof}}$ being the basis functions of the 2D FEM space V_h^1. It is worth remarking that in a two-dimensional setting, the recovered gradient, as the exact and numerical ones, are 2D vectors, therefore $G_h u_h(x_i, y_j) \in V_h^1 \times V_h^1$.

The formula above correctly ensures global continuity of the recovered field, but the spatial distribution of the nodes in 2D excludes the exact interpolation of the local quadratic polynomial. Therefore, to determine its actual values at a specific mesh node $\mathbf{x}_v = (x_i, y_j)$, the fitting of a local quadratic polynomial requires a Discrete Least Squares approximation (DLS), using the values of the numerical solution u_h corresponding to the nodes in the neighborhood of $\mathbf{x}_v$. Figure 2 shows the way in which the node patches are selected according to the position of the selected point $\mathbf{x}_v = (x_i, y_j)$: either the node is internal (left plot), on the edge (central plot) or on a corner of the domain (right plot), the 4 closest elements surrounding $\mathbf{x}_v$ are chosen to create the patch. To mathematically formalize this requirement for interior, edge, and corner nodes simultaneously, we introduce the concept of an *anchor vertex*, denoted as $\tilde{\mathbf{x}}_v \in \mathring{\mathcal{N}}_h$, where $\mathring{\mathcal{N}}_h$ is the set of strictly interior mesh nodes. For any target node $\mathbf{x}_v$, its anchor vertex is defined as:

$$\tilde{\mathbf{x}}_v = \begin{cases} \mathbf{x}_v & \text{if } \mathbf{x}_v \in \mathring{\mathcal{N}}_h \text{ (interior node)}, \\ \arg\min_{\mathbf{y} \in \mathring{\mathcal{N}}_h} \|\mathbf{x}_v - \mathbf{y}\| & \text{if } \mathbf{x}_v \notin \mathring{\mathcal{N}}_h \text{ (boundary or corner node)}. \end{cases} \tag{22}$$

Using this anchor vertex, the element patch ω_v corresponding to the target evaluation node $\mathbf{x}_v$ is strictly defined as the union of all elements $K \in \mathcal{Q}_h$ that share the anchor vertex $\tilde{\mathbf{x}}_v$:

$$\omega_v = \bigcup_{\{K \in \mathcal{Q}_h | \tilde{\mathbf{x}}_v \in K\}} K \tag{23}$$

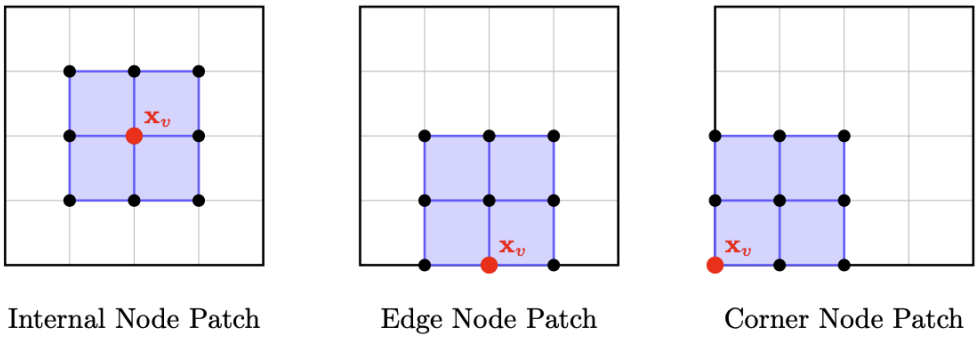

Figure 2: Local Node Patches for a 2D setting on a quadrilateral mesh, considering whether the selected node $\mathbf{x}_v$ is interior (left), on a boundary edge (center), or on a corner (right).

Therefore, each element patch ω_v will contain exactly 9 mesh nodes, as shown in Figure 2, forming the sampling stencil $S_v = \{\mathbf{z}_k\}_{k=1}^{9} = \mathcal{N}_h \cap \omega_v$. Extending then the procedure of the local quadratic polynomial fitting to a two-dimensional setting, the values of the recovered gradient at the mesh nodes are defined as the analytical gradient of the quadratic polynomial fitted over the sampling stencil S_v derived from the element patch ω_v, evaluated at the original target node $\mathbf{x}_v$:

$$G_h u_h(\mathbf{x}_v) = G_h u_h(x_i, y_j) = \nabla p_{\omega_v}(\mathbf{x})\Big|_{\mathbf{x}=\mathbf{x}_v}$$

It is good practice to map the global coordinates into a local system centered at the anchor node $\tilde{\mathbf{x}}_v = (\tilde{x}_i, \tilde{y}_j)$, i.e., using the coordinates $(\xi, \eta) = (x - \tilde{x}_i, y - \tilde{y}_j)$; this helps avoid ill-conditioning when computing the Vandermonde matrix for the DLS procedure. In this local frame, the polynomial $p_{\omega_v} \in \mathbb{P}^2(\omega_v)$ is expressed as:

$$p_{\omega_v}(\xi, \eta) = \mathbf{P}^T\mathbf{c} = [1, \xi, \eta, \xi^2, \xi\eta, \eta^2]^T[c_1, c_2, c_3, c_4, c_5, c_6]$$

and it is derived through the Discrete Least Squares fit on the nodes set S_v, that is finding the vector $\mathbf{c} \in \mathbb{R}^6$ that minimizes the functional $F(\mathbf{c}) = \sum_{k=1}^{9} \left(p_{\omega_v}(\xi_k, \eta_k) - u_h(\mathbf{z}_k)\right)^2$, where (ξ_k, η_k) are the local coordinates of the sampling node $\mathbf{z}_k$. Once the polynomial is obtained, we compute the values of $G_h u_h(\mathbf{x}_v)$ for each target node of the mesh, and replace it in the final version of the estimator (21).

3.4. Mathematical Derivation of the Post-Processing Operator G_h for Quadratic FEM

High-frequency oscillations typical of the solutions of hyperbolic differential problems like Alfvèn waves might require to discretize them with higher-degree Finite Element strategies. Therefore, it is worth pointing out how the recovery gradient is constructed for a case when the numerical solution u_h is obtained with the Finite Element Method on piecewise quadratic polynomials (cfr. with Section 2.2, with $r = 2$).

To preserve the optimal superconvergence properties dictated by the recovery theory [29, 31], the degree of the local fitted polynomial must strictly exceed the degree of the underlying finite element space. Consequently, for a biquadratic $\mathbb{Q}^2$ discretization, the recovery operator must be elevated to fit a local cubic polynomial $p_{\omega_v} \in \mathbb{P}^3$, which requires the determination of 10 unknown coefficients.

Unlike the bilinear case, where the degrees of freedom correspond exclusively to the geometric vertices of the mesh, a $\mathbb{Q}^2$ finite element space distributes its unknowns across element vertices, edge midpoints, and element interiors. Therefore, to ensure a consistent higher-order global reconstruction, the recovered gradient field $G_h u_h$ must be evaluated at all those topological locations.To preserve the optimal superconvergence properties inherent to the recovery operator, the Discrete Least Squares fitting procedure must be strictly restricted to the geometric vertices of the mesh. Rather than constructing individual polynomial fits for edge and interior degrees of freedom, local cubic polynomials are anchored exclusively at the vertex nodes, thereby exploiting their natural topological symmetry.

For each geometric vertex $\tilde{\mathbf{x}}_v \in \mathcal{N}_h$, the corresponding element patch ω_v is constructed dynamically. Starting from the vertex, the algorithm iteratively expands outward by topological rings, gathering all adjacent DOFs until a minimum threshold of sampling points (strictly $n \geq 10$ for a cubic polynomial) is reached. This topological approach provides a robust sampling stencil $S_v = \{\mathbf{z}_k\}_{k=1}^{n}$ that adapts to unstructured boundaries and distorted elements.

Similar to the linear case, the global coordinates are mapped into a local system centered at the vertex, $(\xi, \eta) = (x - \tilde{x}_i, y - \tilde{y}_j)$, to prevent ill-conditioning. In this local frame, the cubic polynomial is expressed as:

$$p_{\tilde{\mathbf{x}}_v}(\xi, \eta) = \mathbf{P}^T\mathbf{c} = [1, \xi, \eta, \xi^2, \xi\eta, \eta^2, \xi^3, \xi^2\eta, \xi\eta^2, \eta^3]^T[c_1, \ldots, c_{10}]$$

and its coefficients are determined by minimizing the functional $F(\mathbf{c}) = \sum_{k=1}^{n} \left(p_{\tilde{\mathbf{x}}_v}(\xi_k, \eta_k) - u_h(\mathbf{z}_k)\right)^2$ over the dynamically gathered node set S_v.

Once these vertex-based polynomials are established, the nodal values of the recovered gradient at any target DOF $\mathbf{x}_v$ are determined through a structured evaluation process. If the target DOF is itself a vertex, the gradient is simply extracted from its own local polynomial. However, if the target DOF lies on an edge or within the interior of an element, its recovered gradient is defined as the arithmetic average of the analytical gradients of polynomials fitted to the adjacent geometric vertices, strictly evaluated at the local specific offset of the target DOF $\mathbf{x}_v$. Figure 3 clarifies the fitting and evaluating procedure for quadrilateral elements. This blending technique ensures that the superconvergent properties achieved at the vertices are smoothly and symmetrically propagated to the rest of the $\mathbb{Q}^2$ degrees of freedom.

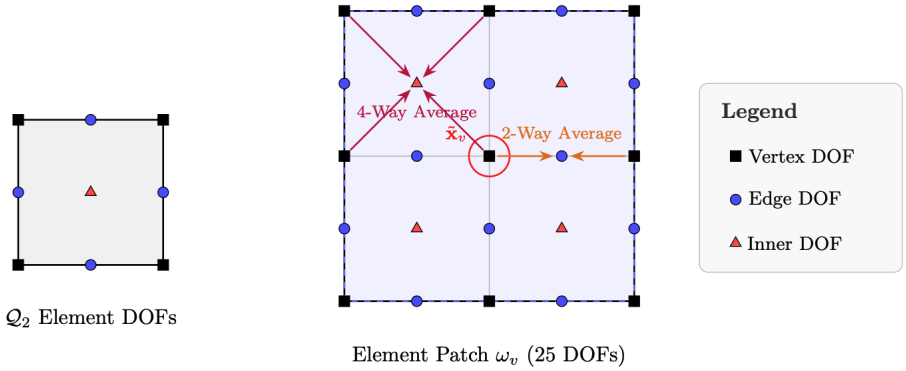

Figure 3: Evaluation of the Recovered Gradient at Vertex DOFs, Edge DOFs and Inner DOF for $\mathbb{Q}^2$-FEM

3.5. Properties of the Recovery-Based Operator and Superconvergence Property

We aim now to prove the effectiveness and asymptotical exactness of the recovery-based spatial error estimator $G_h u_h$ described in Section 3.2, by first explaining the superconvergence property. Following the reasoning by Zhang and Naga [19, 29], we first assess some properties of the PPR operator G_h when applied to a FEM piecewise linear numerical solution $u_h \in V_h^1$:

- The Polynomial Preserving Recovery operator G_h is a linear operator, hence $G_h(a_1 u_{h,1} + a_2 u_{h,2}) = a_1 G_h u_{h,1} + a_2 G_h u_{h,2} \quad \forall a_1, a_2 \in \mathbb{R}, \forall u_{h,1}, u_{h,2} \in V_h^1$.
- G_h is polynomial preserving, that is, given a generic linear interpolant $\Pi_1 p$ of a quadratic polynomial $p \in \mathbb{P}^2$, then $G_h \Pi_1 p = \nabla p$ (or, equivalently, applying the PPR operator G_h to the linear interpolant of p is exactly the same as taking its gradient).
- Under some mild mesh conditions, G_h is bounded in the L^2 norm over the Finite Element space V_h^1 on a local element K, i.e. $\exists C_1 > 0 : \|G_h u\|_{L^2(K)} \leq C_1 |u|_{H^1(K)} \quad \forall u \in V_h^1$.

Furthermore, another important property to mention in order to prove *superconvergence* is related to the gradient of the difference between the numerical solution u_h and the linear interpolant of the corresponding exact solution $I_h u$. The supercloseness property, rigorously proved in [27, Thm. 4.1], recalls that ∇u_h is superconvergent with respect to $\nabla(I_h u)$, more precisely:

$$\|\nabla(I_h u - u_h)\|_{L^2(K)} \leq C_2 h^{1+\rho} \quad \forall K \in \mathcal{Q}_h \tag{24}$$

for some $\rho \in (0, 1)$ and for some $C_2 > 0$ independent of h.

As seen in the literature, the superconvergence of the Polynomial Preserving Recovery (PPR) operator $G_h u_h$ has been rigorously proven in the specific setting of a linear elliptic problem [27, 29]. This proof demonstrates that optimal recovery accuracy is achieved under the assumption of mildly structured meshes and strictly requires sufficient regularity of the exact solution. Provided these conditions are met, the underlying finite element gradient is mathematically guaranteed to superconverge toward the gradient of the exact interpolant, allowing the PPR operator to successfully filter the numerical noise and retrieve the optimal superconvergent rate, as shown in the next result from [29].

Theorem 3.2 (Superconvergence of the PPR-recovered gradient)**.** *Let $u \in W_\infty^3(\Omega)$ be the exact solution of the continuous linear elliptic problem, and let $u_h \in V_h^1$ be its corresponding piecewise linear finite element approximation. Assuming that the discretized mesh $\mathcal{Q}_h$ satisfies the mildly structured condition and the geometric requirements for the boundedness of G_h, there exists a constant $C > 0$, independent of the mesh size h, such that:*

$$\|\nabla u - G_h u_h\|_{L^2(K)} \leq C h^{1+\rho} \|u\|_{W_\infty^3(K)} \quad \forall K \in \mathcal{Q}_h \tag{25}$$

where $\rho \in (0, 1)$ is the same parameter dictating the superconvergence rate of the underlying mesh in (24)*.*

By using Propositions 3.2 and **??**, it is possible to prove the asymptotical exactness of the spatial recovered gradient $G_h u_h$ in the framework of Finite Element with piecewise linear polynomial, hence with $u_h \in V_h^1$. Suppose to consider a generic single quadrilateral element $K \in \mathcal{Q}_h$. Then, applying a first triangular inequality to the exact error of the

gradients, we get:

$$-\|\nabla u - G_h u_h\|_{L^2(K)} + \|G_h u_h - \nabla u_h\|_{L^2(K)} \leq \|\nabla u - \nabla u_h\|_{L^2(K)} \leq \|\nabla u - G_h u_h\|_{L^2(K)} + \|G_h u_h - \nabla u_h\|_{L^2(K)}$$

Therefore, dividing all the terms of the inequality by $\|\nabla u - \nabla u_h\|_{L^2(K)} \neq 0$, replacing the definition 19, we get:

$$-\frac{\|\nabla u - G_h u_h\|_{L^2(K)}}{\|\nabla u - \nabla u_h\|_{L^2(K)}} + \frac{\eta_x(u_h)}{\|\nabla u - \nabla u_h\|_{L^2(K)}} \leq 1 \leq \frac{\|\nabla u - G_h u_h\|_{L^2(K)}}{\|\nabla u - \nabla u_h\|_{L^2(K)}} + \frac{\eta_x(u_h)}{\|\nabla u - \nabla u_h\|_{L^2(K)}}$$

which can be rewritten as:

$$\left| \frac{\eta_x(u_h)}{\|\nabla u - \nabla u_h\|_{L^2(K)}} - 1 \right| \leq \frac{\|\nabla u - G_h u_h\|_{L^2(K)}}{\|\nabla u - \nabla u_h\|_{L^2(K)}}$$

Joining the superconvergence property in Proposition 3.2 with the lower bound proved in [18], which observes that $\exists C_4 > 0 : \|\nabla u - \nabla u_h\|_{L^2(K)} \geq C_4 h$, we get that the right-handed side term can be bounded by:

$$\frac{\|\nabla u - G_h u_h\|_{L^2(K)}}{\|\nabla u - \nabla u_h\|_{L^2(K)}} \leq \frac{C_3 h^{1+\rho}}{C_4 h} \leq C h^{\rho}$$

Therefore, we finally obtain the asymptotical exactness of the spatial error indicator, as:

$$\left| \frac{\eta_x(u_h)}{\|\nabla u - \nabla u_h\|_{L^2(K)}} - 1 \right| \leq C h^{\rho} \xrightarrow{h \to 0} 0$$

proving the result in (21).
Extending these results also to the solution of hyperbolic differential problems is far from trivial, even if this theoretical setting creates a solid baseline where to start from in order to build an a-posteriori recovery-based error indicator in space. The results and the main properties reported in this chapter are verified for hyperbolic differential problems with numerical experiments described in Section 4.

3.6. The Recovery-Based Approach for the Temporal Derivative

In this section we introduce an *a-posteriori* recovery-based error estimator for the temporal part of the natural energy norm of the acoustic wave equation, as defined in (18).
In contrast to the spatial domain which is discretized via a continuous Finite Element space V_h^1, the temporal domain is handled via the Crank-Nicolson time stepping method, as described in Section 2.3. Therefore, the numerical solution u_h^n is naturally discrete in time, being defined only at the specific discrete time instants $t_n, n = 0, ..., N_t$. Because the time domain is handled via finite differences instead of continuous basis functions, the temporal derivative of u_h^n cannot be obtained using analytical differentiation. Thus, we perform a temporal linear interpolation $u_{h,\Delta t}$ of the discrete numerical values $\{u_h^n\}_{n=0}^{N_t}$ on each timeslab $(t^{n-1}, t^n]$ $\forall n = 1, ..., N_t$, in order to be able to differentiate analytically the linearly interpolated numerical solution on each timeslab. This procedure is exactly equivalent to algebraically compute at each timestep t^n the quantity $\frac{\partial u_{h,\Delta t}}{\partial t}(t^n)$ as a backward finite difference quotient utilizing the available finite element snapshots. Specifically, the approximation of the temporal derivative of u_h^n on the timeslab $(t^{n-1}, t^n]$ will be:

$$\frac{\partial u_h^n}{\partial t} \approx \frac{u_h^n - u_h^{n-1}}{\Delta t} = \frac{\partial u_{h,\Delta t}}{\partial t}(t^n) \tag{26}$$

where u_h^n and u_h^{n-1} denote the spatial finite element solutions at the current and previous time steps, respectively. Specific mathematical derivation is performed in Section 3.7.
By definition, this algebraic evaluation yields a discrete field that remains constant over the entire timeslab $(t^{n-1}, t^n]$. Consequently, the resulting proxy for the temporal derivative, $\partial_t u_{h,\Delta t}$, behaves globally as a low-order, piecewise constant field along the time axis. It basically lacks the inter-timeslab continuity and the polynomial degree inherently provided by the spatial Finite Element shape functions. It is precisely this structural discrepancy between spatial smoothness and temporal discontinuity that strictly motivates the introduction of the temporal recovery operator $G_{\Delta t}$, which is designed to artificially filter this piecewise constant noise and restore a higher-order continuous representation in time.

3.7. Mathematical Derivation of the Post-Processing Operator $G_{\Delta t}$

The temporal error indicator $G_{\Delta t}$ is constructed by using the same reasoning as described for the 1D spatial recovery-based operator G_h in Section 3.2. Let $\{t_n\}_{n=0}^{N_t}$ be a partition of the time interval $[0, T]$ into N_t equispaced subintervals of step $\Delta t = \frac{T}{N_t}$. Since the spatial discretization is performed by a conforming finite element space V_h^r, the fully discrete solution is naturally represented by the sequence $\{u_h^n\}_{n=0}^{N_t} \subset V_h^r$. In order to define a continuous-in-time reconstruction, we introduce the Bochner-valued piecewise linear space:

$$V_{\Delta t}^1(V_h^r) = \left\{ v_{h,\Delta t} \in C^0([0,T]; V_h^r) \;\middle|\; v_{h,\Delta t}|_{(t^{n-1}, t^n]} \in \mathbb{P}^1((t^{n-1}, t^n]; V_h^r), \quad n = 1, \ldots, N_t \right\}. \tag{27}$$

This space will contain then all the functions $v_{h,\Delta t} : [0, T] \to V_h^r$ such that $v_{h,\Delta t}(t) \in V_h^r$ $\forall t \in [0, T]$, and, furthermore, they corresponds to piecewise linear polynomials in time. Geometrically, because this temporal reconstruction interpolates linearly between discrete spatial finite element functions, the resulting field over any localized space-time element

$K \times (t^{n-1}, t^n]$ takes the form of a continuous bilinear surface (specifically, a $\mathbb{Q}^1$ polynomial containing space-time cross terms). Similarly, the space of piecewise constant temporal derivatives is:

$$W^0_{\Delta t}(V_h^r) = \left\{ w_{h,\Delta t} \in L^2(0,T;V_h^r) \;\middle|\; w_{h,\Delta t}|_{(t^{n-1},t^n]} \in \mathbb{P}^0((t^{n-1},t^n];V_h^r), \quad n = 1,\dots,N_t \right\}. \tag{28}$$

The continuous-in-time finite element reconstruction $u_{h,\Delta t} \in V^1_{\Delta t}(V_h^r)$ is then defined by temporal linear interpolation of the nodal snapshots $\{u_h^n\}_{n=0}^{N_t}$. Its piecewise constant temporal derivative is denoted by:

$$\partial_t u_{h,\Delta t}|_{(t^{n-1},t^n]} = \frac{u_h^n - u_h^{n-1}}{\Delta t} \in W^0_{\Delta t}(V_h^r). \tag{29}$$

The recovery operator is then defined as:

$$G_{\Delta t} : V^1_{\Delta t}(V_h^r) \longrightarrow V^1_{\Delta t}(V_h^r), \tag{30}$$

acting only in the time variable and leaving the spatial finite element structure unchanged. By linearly interpolating the discrete numerical snapshots $\{u_h^n\}_{n=0}^{N_t}$, the global-in-time numerical solution $u_{h,\Delta t}$ will belong to the space $V^1_{\Delta t}(V_h^r)$ in order to perform the two steps to recover the time derivative. Indeed, at each discrete time level t^n, we fit a local quadratic polynomial $p_{t^n}(t) \in \mathbb{P}^2(V_h^r)$. This notation underlines that this polynomial is quadratic in time, but its coefficients will be obtained by fitting it on the 3-point stencil $K_{t^n} = \{t^{n-1}, t^n, t^{n+1}\}$ through the stencil nodal values of the numerical solution $u_h^{n-1}, u_h^n, u_h^{n+1} \in V_h^r$. This underlines the fact that the coefficients of the polynomial corresponds to specific combinations of FEM functions in V_h^r. For the external time nodes t^0, t^{N_t}, all-left and all-right stencils are considered. Then, we compute the exact analytical derivative of this polynomial, which is evaluated strictly at the node:

$$g^n = \left. \frac{dp_{t^n}(t)}{dt} \right|_{t=t^n}$$

Once the nodal values g^n are computed for all time steps, the global continuous-in-time recovered derivative is constructed by using these values as coefficients of the linear combination of the standard 1D linear shape functions (hat functions in time) $\varphi_n(t)$ associated with the temporal grid $\{t^n\}_{n=0}^{N_t}$:

$$G_{\Delta t} u_{h,\Delta t}(t) = \sum_{n=0}^{N_t} g^n \varphi_n(t) \tag{31}$$

This procedure resembles the one described for spatial FEM in Section 3.2, but it is adapted for the temporal setting, where it is more frequent to use time-stepping or Finite Difference techniques to approximate the temporal derivative $\partial_t u$. This recovery-based process let us define the temporal error indicator $\forall n \in \mathbb{N}$:

$$\eta_t(u_h^n) = \left(\sum_{K \in \mathcal{Q}_h} \| G_{\Delta t} u_{h,\Delta t}(t^n) - \partial_t u_{h,\Delta t}(t^n) \|^2_{L^2(K)} \right)^{1/2} \tag{32}$$

It is important to notice that, recalling the definition of the natural energy norm of the error for the acoustic wave equation in (18), this quantity is evaluated at the final time, whilst the recovery error indicators for space and time formalized earlier are defined on subintervals $[x_{i-1}, x_i]$ and timeslabs $[t^n, t^{n+1}]$. Therefore, in order to relate the indicator to the actual natural energy norm, it is necessary to regularize the energy norm to an averaged version in time over a small time window close to the final time $(T - m\Delta t, T]$ for some $m \in \mathbb{N}$, and compute the error by using the Root Mean Square (RMS) metric over time:

$$\mathrm{RMS}_t(\|e\|_{L^2(\Omega)}) = \left(\frac{1}{m\Delta t} \int_{T-m\Delta t}^{T} \|e(\cdot,t)\|^2_{L^2(\Omega)} dt \right)^{1/2} \tag{33}$$

We notice also that, as the temporal step size vanishes $\Delta t \to 0$, the RMS norm converges to the value of the error at the final time $t = T$, respecting our intention of approximating the error in the natural energy norm, as seen in (18). By using the RMS metric, we ensure that the subsequent superconvergence and asymptotic exactness analyses are evaluated against the true, time-averaged behavior of the temporal derivative, rather than a potentially biased single-instance snapshot. Since the Crank-Nicolson time stepping method is second-order in time, but the numerical derivative $\partial_t u_{h,\Delta t} \in W^0_{\Delta t}(V_h^r)$ is only piecewise constant, the behavior of the convergence of the temporal derivative of the error degrades to the one of a backward Finite Difference scheme (order $O(\Delta t)$), namely:

$$\left\| \frac{\partial u}{\partial t}(\cdot,t^n) - \partial_t u_{h,\Delta t}(\cdot,t^n) \right\|_{L^2(\Omega)} \approx O(\Delta t) \tag{34}$$

Therefore, the purpose of the recovered estimator $G_{\Delta t}$ is to create a recovered version of the temporal derivative which allows the RMS of the *a-posteriori* temporal error estimate $\|G_{\Delta t} u_{h,\Delta t}(t^n) - \partial_t u_{h,\Delta t}(t^n)\|_{L^2(\Omega)}$ to converge with the same order. Finally, in order to retrieve the correct numerical orders for the RMS errors, a Simpson quadrature rule in time will be used to approximate the temporal integral in (33).

3.8. Asymptotic Exactness of the Temporal Recovery-Based Estimator $G_{\Delta t}$

We aim now to prove the asymptotic exactness of the temporal error estimator. The rigorous superconvergence framework introduced by Zhang and Naga [19, 29] focuses mainly on spatial finite element approximations. Therefore, the reasoning will here be extended to the temporal domain in the fully discrete setting and a more precise and formal setting will be estabilished to assess the superconvergence.
Following the reasoning in Section 3.5, we start by stating and proving the properties of linearity, polynomial preservation, and boundedness of the temporal recovery-based operator $G_{\Delta t}$ needed for getting the superconvergence property. Before detailing the formal proofs, it is important to clarify how the spatial dependency of the discrete solutions is handled within this framework. Since the continuous-in-time reconstruction $u_{h,\Delta t}$ is defined in the Bochner space $V^1_{\Delta t}(V^r_h)$, the temporal recovery operator $G_{\Delta t}$ acts exclusively on the time variable, leaving the spatial finite element structure unaltered. Consequently, the subsequent properties are initially established in the strictly one-dimensional temporal domain for almost every spatial point $x \in \Omega$. The global space-time estimates are then obtained by integrating these local bounds over the spatial domain Ω. This exchange of integration order is rigorously justified by Fubini's Theorem, thanks to the piecewise polynomial regularity and measurability of the underlying finite element spaces.

Theorem 3.3 (Linearity of the Temporal Recovery-Based Operator)**.** *The temporal recovery-based operator $G_{\Delta t}$ as constructed in 3.7 is linear, i.e. $G_{\Delta t}(\alpha u_{h,\Delta t} + \beta v_{h,\Delta t}) = \alpha G_{\Delta t} u_{h,\Delta t} + \beta G_{\Delta t} v_{h,\Delta t} \quad \forall \alpha, \beta \in \mathbb{R}$ and $\forall u_{h,\Delta t}, v_{h,\Delta t} \in V^1_{\Delta t}(V^r_h)$.*

Proof. Let $w_{h,\Delta t}(t) = \alpha u_{h,\Delta t}(t) + \beta v_{h,\Delta t}(t)$. Since $V^1_{\Delta t}(V^r_h)$ is a vector space, it naturally follows that $w_{h,\Delta t} \in V^1_{\Delta t}(V^r_h)$. Then, for every discrete time node t^n, we get: $w^n_h = \alpha u^n_h + \beta v^n_h$. Since $G_{\Delta t} w_{h,\Delta t}(t) \in V^1_{\Delta t}(V^r_h)$, it can be written as in (31), where the coefficient of the basis function $\varphi_n(t)$ in the linear combination is defined as:

$$g^n[w_{h,\Delta t}] := G_{\Delta t} w_{h,\Delta t}(t^n) = \left.\frac{dp_{t^n}[w_{h,\Delta t}](t)}{dt}\right|_{t=t^n}$$

where $p_{t^n}[w_{h,\Delta t}] \in \mathbb{P}^2(V^r_h)$ is the local quadratic polynomial which fits exactly the 3-point stencil values $w^{n-1}_h, w^n_h, w^{n+1}_h$ as described in Section 3.7. Let S_n be the set of the three temporal indices corresponding to the stencil of node t^n (e.g., $S_n = \{n-1, n, n+1\}$ for interior nodes, and appropriately shifted for boundaries). By associating the standard Lagrange quadratic basis functions $\{L_k(t)\}_{k \in S_n}$ to the corresponding time nodes of the stencil, the fitted polynomial can be uniquely expressed as:

$$p_{t^n}[w_{h,\Delta t}](t) = \sum_{k \in S_n} w^k_h L_k(t) = \sum_{k \in S_n} (\alpha u^k_h + \beta v^k_h) L_k(t) = \alpha \sum_{k \in S_n} u^k_h L_k(t) + \beta \sum_{k \in S_n} v^k_h L_k(t) = \alpha p_{t^n}[u_{h,\Delta t}](t) + \beta p_{t^n}[v_{h,\Delta t}](t)$$

Thanks to the linearity of the exact analytical derivative, we get that for all the time nodes t^n, with $n = 0, ..., N_t$:

$$g^n[w_{h,\Delta t}] = \left.\frac{dp_{t^n}[w_{h,\Delta t}](t)}{dt}\right|_{t=t^n} = \alpha \left.\frac{dp_{t^n}[u_{h,\Delta t}](t)}{dt}\right|_{t=t^n} + \beta \left.\frac{dp_{t^n}[v_{h,\Delta t}](t)}{dt}\right|_{t=t^n} = \alpha g^n[u_{h,\Delta t}] + \beta g^n[v_{h,\Delta t}]$$

Therefore, we guarantee the global linearity of the operator by substituting these nodal values back into the definition of the temporal recovery-based operator (31):

$$G_{\Delta t}(\alpha u_{h,\Delta t} + \beta v_{h,\Delta t})(t) = \sum_{n=0}^{N_t} g^n[w_{h,\Delta t}]\varphi_n(t) = \alpha \sum_{n=0}^{N_t} g^n[u_{h,\Delta t}]\varphi_n(t) + \beta \sum_{n=0}^{N_t} g^n[v_{h,\Delta t}]\varphi_n(t) = \alpha G_{\Delta t} u_{h,\Delta t}(t) + \beta G_{\Delta t} v_{h,\Delta t}(t).$$

□

Theorem 3.4 (Polynomial Preservation of the Temporal Recovery-Based Operator)**.** *The temporal recovery-based operator $G_{\Delta t}$ preserves quadratic polynomials, i.e. $G_{\Delta t}(I_{\Delta t} p) = \partial_t p \quad \forall p \in \mathbb{P}^2(V^r_h)$, where $I_{\Delta t} p \in V^1_{\Delta t}(V^r_h)$ is the exact temporal linear interpolant of p.*

Proof. Let $p(t) \in \mathbb{P}^2(V^r_h)$ be an arbitrary exact quadratic polynomial in time with coefficients in V^r_h, and let $w_{h,\Delta t}(t) = I_{\Delta t} p(t) \in V^1_{\Delta t}(V^r_h)$ be its continuous linear interpolant on the temporal partition. By definition of exact nodal interpolation, for every discrete time node t^k, the nodal values coincide strictly with the exact polynomial: $w^k_h = I_{\Delta t} p(t^k) = p(t^k)$. Following the construction of the operator, at a generic time node t^n, a local quadratic polynomial $p_{t^n}[w_{h,\Delta t}] \in \mathbb{P}^2(V^r_h)$ is fitted to exactly interpolate the 3-point temporal stencil. Let S_n denote the set of the three temporal indices corresponding to the specific stencil of node t^n. Since $w^k_h = p(t^k)$ for all $k \in S_n$, the fitted polynomial perfectly matches the exact polynomial $p(t)$ at three distinct temporal nodes. By the unisolvence theorem of polynomial interpolation, a polynomial of degree 2 is uniquely determined by its evaluation at three distinct points. Consequently, the locally fitted polynomial strictly equates to the original continuous polynomial over the entire domain: $p_{t^n}[w_{h,\Delta t}](t) \equiv p(t)$.
Evaluating the analytical time derivative of the fitted polynomial precisely at the target node t^n yields the recovered nodal derivative:

$$g^n[w_{h,\Delta t}] = \left.\frac{dp_{t^n}[w_{h,\Delta t}](t)}{dt}\right|_{t=t^n} = \left.\frac{dp(t)}{dt}\right|_{t=t^n} = \partial_t p(t^n)$$

The global continuous-in-time recovered derivative is then assembled by interpolating these superconvergent nodal values using the standard 1D linear shape functions $\varphi_n(t)$:

$$G_{\Delta t}(I_{\Delta t}p)(t) = \sum_{n=0}^{N_t} g^n[w_{h,\Delta t}]\varphi_n(t) = \sum_{n=0}^{N_t} \partial_t p(t^n)\varphi_n(t)$$

Since the initial exact polynomial $p(t) \in \mathbb{P}^2(V_h^r)$, its continuous derivative will be a linear function, i.e., $\partial_t p(t) \in \mathbb{P}^1(V_h^r)$. Because the finite element space $V_{\Delta t}^1(V_h^r)$ exactly interpolates linear functions, applying the nodal interpolation to a function that already belongs to $\mathbb{P}^1(V_h^r)$ recreates the original function with zero approximation error, as $\mathbb{P}^1(V_h^r) \subset V_{\Delta t}^1(V_h^r)$. Therefore, the linear combination reduces perfectly to the exact derivative:

$$\sum_{n=0}^{N_t} \partial_t p(t^n)\varphi_n(t) = \partial_t p(t)$$

which proves that $G_{\Delta t}(I_{\Delta t}p) = \partial_t p$. □

Theorem 3.5 (L^2-Boundedness of the Temporal Recovery-Based Operator)**.** *Let $I_n = (t^{n-1}, t^n]$ be a specific timeslab and $\omega_n = I_{n-1} \cup I_n \cup I_{n+1}$ be its associated macro-timeslab. The temporal recovery-based operator $G_{\Delta t}$ satisfies the local space-time boundedness property:*

$$\|G_{\Delta t}u_{h,\Delta t}\|_{L^2(I_n;L^2(\Omega))} \leq C\|\partial_t u_{h,\Delta t}\|_{L^2(\omega_n;L^2(\Omega))}$$

where $C > 0$ is a constant strictly independent of the time step Δt, and $\partial_t u_{h,\Delta t} \in W_{\Delta t}^0(V_h^r)$ denotes the piecewise constant discrete temporal derivative as defined in (26).

Proof. Since the continuous-in-time reconstruction $u_{h,\Delta t}$ belongs to the Bochner space $V_{\Delta t}^1(V_h^r)$, we first establish the boundedness in the strictly one-dimensional temporal domain for almost every spatial point $\mathbf{x} \in \Omega$. Let $u_h^k(\mathbf{x})$ denote the pointwise evaluation of the nodal snapshot $u_h^k \in V_h^r$. To simplify the algebraic notation, let $\delta_t u_h^k(\mathbf{x}) = (u_h^k(\mathbf{x}) - u_h^{k-1}(\mathbf{x}))/\Delta t$ represent the constant value of the discrete temporal derivative on the timeslab I_k. Therefore, its squared L^2-norm over the timeslab equates to $\|\partial_t u_{h,\Delta t}(\mathbf{x},\cdot)\|_{L^2(I_k)}^2 = \Delta t(\delta_t u_h^k(\mathbf{x}))^2$.
At a strictly internal time node t^n (where $0 < n < N_t$), the recovered nodal derivative $g^n(\mathbf{x})$ is evaluated as the exact analytical derivative of the local quadratic polynomial $p_{t^n}(\mathbf{x},t)$ evaluated at $t = t^n$. Due to the uniform spacing of the temporal grid, this expression reduces analytically to the central difference quotient:

$$g^n(\mathbf{x}) = \frac{u_h^{n+1}(\mathbf{x}) - u_h^{n-1}(\mathbf{x})}{2\Delta t} = \frac{1}{2}\left(\frac{u_h^{n+1}(\mathbf{x}) - u_h^n(\mathbf{x})}{\Delta t} + \frac{u_h^n(\mathbf{x}) - u_h^{n-1}(\mathbf{x})}{\Delta t}\right) = \frac{1}{2}(\delta_t u_h^{n+1}(\mathbf{x}) + \delta_t u_h^n(\mathbf{x}))$$

Applying the fundamental algebraic inequality $(a+b)^2 \leq 2a^2 + 2b^2$, the square of the recovered nodal derivative is bounded by:

$$(g^n(\mathbf{x}))^2 \leq \frac{1}{2}\left((\delta_t u_h^{n+1}(\mathbf{x}))^2 + (\delta_t u_h^n(\mathbf{x}))^2\right)$$

Within a generic internal interval I_n, the globally recovered derivative evaluated at $\mathbf{x}$ is exactly the linear interpolation $G_{\Delta t}u_{h,\Delta t}(\mathbf{x},t)\big|_{I_n} = g^{n-1}(\mathbf{x})\varphi_{n-1}(t) + g^n(\mathbf{x})\varphi_n(t)$. Integrating its square over I_n equates to the standard 1D finite element mass matrix evaluation:

$$\|G_{\Delta t}u_{h,\Delta t}(\mathbf{x},\cdot)\|_{L^2(I_n)}^2 = \int_{t^{n-1}}^{t^n} (g^{n-1}(\mathbf{x})\varphi_{n-1}(t) + g^n(\mathbf{x})\varphi_n(t))^2 dt = \frac{\Delta t}{3}\left((g^{n-1}(\mathbf{x}))^2 + g^{n-1}(\mathbf{x})g^n(\mathbf{x}) + (g^n(\mathbf{x}))^2\right)$$

Applying Young's inequality, $ab \leq \frac{1}{2}a^2 + \frac{1}{2}b^2$, to decouple the cross term, the integral is strictly bounded by:

$$\|G_{\Delta t}u_{h,\Delta t}(\mathbf{x},\cdot)\|_{L^2(I_n)}^2 \leq \frac{\Delta t}{2}\left((g^{n-1}(\mathbf{x}))^2 + (g^n(\mathbf{x}))^2\right)$$

Assuming both t^{n-1} and t^n are internal nodes, we substitute the discrete difference bounds derived previously into this integral, yielding:

$$\|G_{\Delta t}u_{h,\Delta t}(\mathbf{x},\cdot)\|_{L^2(I_n)}^2 \leq \frac{\Delta t}{4}\left((\delta_t u_h^n(\mathbf{x}))^2 + (\delta_t u_h^{n-1}(\mathbf{x}))^2 + (\delta_t u_h^{n+1}(\mathbf{x}))^2 + (\delta_t u_h^n(\mathbf{x}))^2\right)$$

Recalling the identity $\Delta t(\delta_t u_h^k(\mathbf{x}))^2 = \|\partial_t u_{h,\Delta t}(\mathbf{x},\cdot)\|_{L^2(I_k)}^2$, the inequality is rewritten in terms of the local temporal norms:

$$\|G_{\Delta t}u_{h,\Delta t}(\mathbf{x},\cdot)\|_{L^2(I_n)}^2 \leq \frac{1}{4}\|\partial_t u_{h,\Delta t}(\mathbf{x},\cdot)\|_{L^2(I_{n-1})}^2 + \frac{1}{2}\|\partial_t u_{h,\Delta t}(\mathbf{x},\cdot)\|_{L^2(I_n)}^2 + \frac{1}{4}\|\partial_t u_{h,\Delta t}(\mathbf{x},\cdot)\|_{L^2(I_{n+1})}^2 \leq \frac{1}{2}\|\partial_t u_{h,\Delta t}(\mathbf{x},\cdot)\|_{L^2(\omega_n)}^2$$

For the boundary timeslabs I_1 and I_{N_t}, the adjacent nodal derivatives ($g^0(\mathbf{x})$ and $g^{N_t}(\mathbf{x})$) are evaluated using one-sided, three-point stencils rather than central differences. Expanding these asymmetrical difference quotients yields the same structural inequality, simply modifying the stability constant. Thus, for any timeslab I_n, there exists a generic constant $C > 0$ such that the local temporal bound holds.

To formalize this bound with respect to the spatial domain, we integrate both sides of the inequality over Ω:

$$\int_\Omega \|G_{\Delta t} u_{h,\Delta t}(\mathbf{x},\cdot)\|^2_{L^2(I_n)} d\mathbf{x} \le C^2 \int_\Omega \|\partial_t u_{h,\Delta t}(\mathbf{x},\cdot)\|^2_{L^2(\omega_n)} d\mathbf{x}$$

Expanding the temporal norms results in nested spatial and temporal integrals. By applying Fubini's Theorem, which is strictly justified since the Bochner space functions are measurable on $\Omega \times (0,T)$, to exchange the order of integration, we obtain:

$$\int_{I_n} \left(\int_\Omega |G_{\Delta t} u_{h,\Delta t}(\mathbf{x},t)|^2 d\mathbf{x} \right) dt \le C^2 \int_{\omega_n} \left(\int_\Omega |\partial_t u_{h,\Delta t}(\mathbf{x},t)|^2 d\mathbf{x} \right) dt$$

Recognizing the inner integrals directly as the spatial $L^2(\Omega)$ norms, the nested integrals condense into the desired space-time formulation:

$$\|G_{\Delta t} u_{h,\Delta t}\|^2_{L^2(I_n;L^2(\Omega))} \le C^2 \|\partial_t u_{h,\Delta t}\|^2_{L^2(\omega_n;L^2(\Omega))}$$

Taking the square root of both sides concludes the proof, yielding a generic stability constant C (specifically, $C = 1/\sqrt{2}$ for strictly internal patches), which remains strictly independent of the temporal discretization parameter Δt. □

Once the properties above have been analysed, we move on to assess the superconvergence of $G_{\Delta t} u_{h,\Delta t}$ with respect to $\partial_t u$. We reintroduce the exact temporal linear interpolant $I_{\Delta t} u \in V^1_{\Delta t}(L^2(\Omega))$, denoting the continuous piecewise linear interpolation in time of the exact solution sampled at the time nodes. By applying the triangle inequality, the error splits into two different terms:

$$\|\partial_t u - G_{\Delta t} u_{h,\Delta t}\|_{L^2(I_n;L^2(\Omega))} \le \|\partial_t u - G_{\Delta t}(I_{\Delta t} u)\|_{L^2(I_n;L^2(\Omega))} + \|G_{\Delta t}(I_{\Delta t} u - u_{h,\Delta t})\|_{L^2(I_n;L^2(\Omega))} \tag{35}$$

For the first term, we evaluate the interpolation error of the recovery operator applied to exact nodal data. We use the polynomial-preserving property of $G_{\Delta t}$. Since $G_{\Delta t} I_{\Delta t} p = \partial_t p$ for every quadratic polynomial in time, the operator $\partial_t - G_{\Delta t} I_{\Delta t}$ vanishes on $\mathbb{P}^2(L^2(\Omega))$. Hence, by the standard one-dimensional interpolation estimate in time, applied with values in the Hilbert space $L^2(\Omega)$, we obtain the bound for the interpolation error:

$$\|\partial_t u - G_{\Delta t}(I_{\Delta t} u)\|_{L^2(I_n;L^2(\Omega))} \le C_1 \Delta t^2 \|\partial_{ttt} u\|_{L^2(\omega_n;L^2(\Omega))}$$

provided that $u \in H^3(\omega_n; L^2(\Omega))$. The estimate is written on the patch ω_n because the recovered nodal values are constructed from three-point temporal stencils. Near the initial and final time levels, the same estimate holds by using the corresponding one-sided stencils.

For the second term, we apply the local space-time L^2-boundedness property of the temporal operator proved earlier in Theorem 3.5:

$$\|G_{\Delta t}(I_{\Delta t} u - u_{h,\Delta t})\|_{L^2(I_n;L^2(\Omega))} \le C_2 \|\partial_t (I_{\Delta t} u - u_{h,\Delta t})\|_{L^2(\omega_n;L^2(\Omega))}$$

The right-hand side represents the discrete, piecewise constant temporal derivative of the numerical error over the macro-timeslab ω_n. We assume the following temporal supercloseness estimate for the fully discrete Crank-Nicolson finite element solution:

$$\|\partial_t (I_{\Delta t} u - u_{h,\Delta t})\|_{L^2(\omega_n;L^2(\Omega))} \le C_{CN}(h^{r+1} + \Delta t^2) \tag{36}$$

This estimate accounts for both the spatial finite element error and the second-order temporal consistency of the Crank-Nicolson scheme. It is important to emphasize that establishing this temporal supercloseness result for the fully discrete temporal Crank-Nicolson and spatial finite element approximation is a complex task requiring extensive energy-based stability arguments; thus, we formally adopt this estimate as a foundational assumption for our theoretical framework. Substituting this supercloseness bound into the boundedness inequality provides the final bound for the second term:

$$\|G_{\Delta t}(I_{\Delta t} u - u_{h,\Delta t})\|_{L^2(I_n;L^2(\Omega))} \le C_2 C_{CN}(h^{r+1} + \Delta t^2)$$

Substituting these two bounds back into (35) gives us:

$$\|\partial_t u - G_{\Delta t} u_{h,\Delta t}\|_{L^2(I_n;L^2(\Omega))} \le C(\Delta t^2 + h^{r+1})$$

In particular, for piecewise linear finite elements, $r = 1$, and under the balanced refinement regime $h \sim \Delta t$, one obtains that the recovered temporal derivative achieves a superconvergence rate of:

$$\|\partial_t u - G_{\Delta t} u_{h,\Delta t}\|_{L^2(I_n;L^2(\Omega))} \le C\Delta t^2 = \mathcal{O}(\Delta t^2)$$

This shows that the recovered temporal derivative is one order more accurate than the piecewise constant backward difference derivative $\partial_t u_{h,\Delta t}$, whose error is typically of order $\mathcal{O}(\Delta t)$, under the assumptions of regularity of the exact solution and supercloseness, as given in (36).

This result allows us to finally prove the asymptotic exactness of the temporal estimator. The actual temporal discretization error, when considering the piecewise constant algebraic derivative $\partial_t u_{h,\Delta t}$, converges with a linear rate $\mathcal{O}(\Delta t)$ when measured in the natural space-time Bochner norm. Therefore, by assuming a lower bound for the *a-priori* convergence result $\|\partial_t u - \partial_t u_{h,\Delta t}\|_{L^2(I_n;L^2(\Omega))} \ge C\Delta t$ and evaluating these continuous quantities over a generic timeslab $I_n = (t^{n-1}, t^n]$, the deviation of the local effectivity index from 1 is rigorously bounded as follows:

$$\left| \frac{\|G_{\Delta t} u_{h,\Delta t} - \partial_t u_{h,\Delta t}\|_{L^2(I_n;L^2(\Omega))}}{\|\partial_t u - \partial_t u_{h,\Delta t}\|_{L^2(I_n;L^2(\Omega))}} - 1 \right| \le \frac{\|\partial_t u - G_{\Delta t} u_{h,\Delta t}\|_{L^2(I_n;L^2(\Omega))}}{\|\partial_t u - \partial_t u_{h,\Delta t}\|_{L^2(I_n;L^2(\Omega))}} \approx \frac{\mathcal{O}(\Delta t^2)}{\mathcal{O}(\Delta t)} = \mathcal{O}(\Delta t) \tag{37}$$

Since the bounding term $\mathcal{O}(\Delta t)$ strictly vanishes as the temporal step $\Delta t \to 0$, the local effectivity index tends exactly to 1, which analytically proves that the temporal recovery-based estimator is asymptotically exact.

3.9. The Recovery-Based Approach for the Recovered Solution in the L^2 Norm

In this last subsection of the recovery-based error estimators for hyperbolic differential problems, we describe how to proceed when the natural energy norm of the considered problem contains inside the L^2 norm of the error, namely $\|u - u_h\|_{L^2(\Omega)}$. The main difference between this technique and the one used for the spatial and temporal derivatives in the previous sections is that the latter was based on the Superconvergent Patch Recovery (SPR) by Zienkiewicz and Zhu [30] applied on the stresses/gradients; the former instead aims to check how the SPR performs if it is applied to the actual displacement/solution. We follow the approach of Li and Wiberg in [26] and, for the sake of simplicity, we will consider the framework of a linear 2D elliptic problem, to utilize the main result of superconvergence as done in [26].
We start by considering a quadrilateral mesh $\mathcal{Q}_h$ of the open, bounded domain $\Omega \subset \mathbb{R}^2$, and let $u_h \in V_h^r$ be the numerical solution of (2) solved with the Galerkin Finite Element Method on piecewise polynomials of degree r, as described in Section 2. The goal is to construct a recovery-based error operator $R_h : V_h^r \to V_h^{r+1}$ such that $u_h^* := R_h u_h$ approximates the exact solution u better than the actual numerical solution u_h does, since it gains a higher polynomial degree than u_h. This leads to the following definition of the error indicator:

$$\eta_s(u_h) = \left(\sum_{K \in \mathcal{Q}_h} \|u_h^* - u_h\|_{L^2(K)}^2 \right)^{1/2} \tag{38}$$

which should asymptotically converge to the actual L^2-norm of the error $\|u - u_h\|_{L^2(\Omega)}$ as the mesh size $h \to 0$.
The construction of the recovered solution u_h^* starts with the definition of the space V_h^{r+1}:

$$V_h^{r+1} = \left\{ v_h \in C^0(\bar{\Omega}) \mid v_h|_K \circ F_K \in \mathbb{Q}_{r+1}(\hat{K}) \quad \forall K \in \mathcal{Q}_h,\ v_h|_{\partial\Omega} = 0 \right\},$$

with $F_K : \hat{K} \to K$ being the affine transformation that maps each point of the reference square $\hat{K} = [-1, 1]^2$ into the corresponding element K. Let M_{dof} be the dimension of V_h^{r+1} and let $\{\psi_i(\mathbf{x})\}_{i=1}^{M_{dof}}$ be the corresponding global Lagrangian nodal basis functions. Then, we can rewrite the recovered solution u_h^* as:

$$u_h^* = R_h u_h = \sum_{i=1}^{M_{dof}} \bar{u}_i^* \psi_i(\mathbf{x}) \tag{39}$$

where the coefficients $\bar{u}_i^*$ represent the nodal values of the recovered solution evaluated at the degrees of freedom (DOFs) $\mathbf{x}_i$ of the enriched space V_h^{r+1}. To determine the coefficients $\bar{u}_i^*$ and uniquely define the global recovered field u_h^*, we categorize the degrees of freedom of the enriched space V_h^{r+1} into primary geometric vertices and intermediate nodes (located on edges or within element interiors, as done in Figure 2). For any DOF corresponding to a geometric vertex $\mathbf{x}_v$, we enforce a strict nodal preservation condition, setting $\bar{u}_v^* = u_h(\mathbf{x}_v)$.
To evaluate the remaining intermediate DOFs, we construct a higher-degree local polynomial at each geometric vertex. For a given vertex $\mathbf{x}_v$, a topological patch ω_v is defined by initially aggregating all elements sharing this vertex. Over this assembled patch ω_v, we construct a local continuous polynomial $p_{\omega_v} \in \mathbb{P}^{r+1}$. The coefficients of this polynomial are determined by performing a Discrete Least Squares (DLS) minimization. At this stage, it is necessary to select the specific sampling points within ω_v where the functional will be evaluated. Following the theory established by Wiberg and Li [26], this recovery procedure yields an asymptotically exact error estimate. However, this strictly requires fitting the local polynomial exactly at the superconvergent points of the primal finite element solution. To capture these points, standard macro-patches are constructed symmetrically. A typical patch consists of a central mesh element surrounded by its immediate neighbors, such as a 3×3 grid of quadrilaterals. Wiberg and Li sampled the raw numerical solution u_h at these superconvergent nodes $\mathbf{z}_k$ within the patch. Through this approach, they successfully demonstrated superconvergence for linear elliptic problems [26].
Nevertheless, this primal recovery method has a severe structural constraint. Unlike the gradient field, the primary variable u_h lacks superconvergent points when computed via piecewise linear finite elements ($\mathbb{P}^1$ or $\mathbb{Q}^1$). These points exist neither within the element interior nor on its boundaries. Consequently, this specific L^2 recovery strategy cannot be applied to linear meshes. It is strictly restricted to higher-order discretizations, requiring finite element spaces of degree $r \geq 2$.
As done in the procedure to build the 2D spatial recovered gradient in Section 3.2, to guarantee the algebraic stability of the inversion process and avoid ill-conditioning in the resultant linear system, the global coordinates of the sampling points $\mathbf{z}_k = (x_k, y_k)$ are mapped to a locally scaled coordinate system centered at the vertex $\mathbf{x}_v = (x_v, y_v)$. The local coordinates are defined as $\xi_k = (x_k - x_v)/h$ and $\eta_k = (y_k - y_v)/h$, where h is a characteristic scaling parameter defined as the maximum bounding box dimension of the patch. The local polynomial is thus expressed as $p_{\omega_v}(\xi, \eta) = \mathbf{P}(\xi, \eta)^T \mathbf{c}_v$, where $\mathbf{P}$ is the polynomial basis vector and $\mathbf{c}_v$ is the vector of unknown coefficients.
The discrete least-squares functional to be minimized is formulated as:

$$F(\mathbf{c}_v) = \sum_{k=1}^{n_v} \left(\mathbf{P}(\xi_k, \eta_k)^T \mathbf{c}_v - u_h(\mathbf{z}_k) \right)^2 \tag{40}$$

where n_v denotes the total number of sampling DOFs encompassed by the patch ω_v. Imposing the stationarity condition $\partial F / \partial \mathbf{c}_v = \mathbf{0}$ yields the standard system of normal equations:

$$\left(\sum_{k=1}^{n_v} \mathbf{P}(\xi_k, \eta_k) \mathbf{P}(\xi_k, \eta_k)^T \right) \mathbf{c}_v = \sum_{k=1}^{n_v} \mathbf{P}(\xi_k, \eta_k) u_h(\mathbf{z}_k) \tag{41}$$

which can be compactly rewritten in matrix form as $\mathbf{A}^T\mathbf{A}\mathbf{c}_v = \mathbf{A}^T\mathbf{b}$. Solving this linear system provides the optimal coefficients $\mathbf{c}_v$, thereby fully defining the higher-order local polynomial p_{ω_v} associated with the vertex $\mathbf{x}_v$. Once the local polynomial p_{ω_v} is fully defined for every geometric vertex in the mesh, the remaining degrees of freedom of the enriched space must be evaluated. For any intermediate node $\mathbf{x}_i$ (located either on the edges or within the interior of a specific mesh element K), its nodal value $\bar{u}_i^*$ is computed as the arithmetic mean of the evaluations of the local polynomials associated with all the geometric vertices comprising that element. Mathematically, this averaging procedure is expressed as:

$$\bar{u}_i^* = \frac{1}{N_V^K} \sum_{v \in \mathcal{V}(K)} p_{\omega_v}(\mathbf{x}_i) \tag{42}$$

where $\mathcal{V}(K)$ represents the set of geometric vertices defining the element K, and N_V^K is the total number of such vertices. By enforcing exact nodal interpolation at the primary vertices and applying this polynomial averaging at the intermediate nodes, the global recovered field u_h^* is uniquely determined and maintains strict C^0-continuity across all element boundaries. Once u_h^* has been constructed, it is replaced into (38) to compute the *a-posteriori* estimator.
It is worth concluding the chapter by explaining that the results here derived, especially the ones related to the spatial gradient in Section 3.2 and to the actual Finite Element solution in this Section, were described and analyzed in the framework of a linear elliptic problem. Therefore, the extension of these rigorous superconvergence proofs to hyperbolic differential equations is theoretically challenging. Since the analytical properties of the wave equation differ fundamentally from the elliptic setting, a formal proof of superconvergence for these recovered estimators is not directly available. Consequently, the actual performance and the superconvergent behavior of the recovery strategies proposed in the hyperbolic framework will be assessed through numerical experiments. Nevertheless, this theoretical background was strictly necessary. It provides the mathematical foundation required to conceptualize the recovery operators, justify the mechanics of their construction, and set the starting point of our methodology. By establishing how these post-processing techniques filter discretization errors in the standard elliptic case, we can properly investigate their effectiveness when applied to hyperbolic problems like the acoustic wave equation, or to more complex physical configurations such as Alfvén waves.

4. Numerical Results for the 1D and 2D Wave Equation

This section presents the numerical results concerning the performance of the recovery-based error estimators applied to the acoustic wave equation. Specifically, we discretize the one- and two-dimensional hyperbolic problem introduced in Section 2 using continuous piecewise linear finite elements ($r = 1$) in space and the Crank-Nicolson scheme in time. The numerical solution u_h obtained from this discretization is then utilized to compute both the true discretization errors against manufactured exact solutions $u(x, t)$ and the corresponding a-posteriori error indicators. The primary objective is to verify whether the spatial and temporal recovery operators, G_h and $G_{\Delta t}$, correctly capture the asymptotic behavior and the magnitude of the true discretization error in the energy norm, as defined in (18).
The numerical experiments are structured into four distinct test cases: two dedicated to one-dimensional wave propagation and two focusing on two-dimensional domains. All simulations and post-processing recovery procedures have been implemented entirely in Python, relying on the open-source computing platform FEniCSx [3, 10] for computing the finite element solution at each timestep.
To provide a fair assessment of the error dynamics without being biased by specific zero-crossing instances of the oscillatory wave, the error norms are systematically evaluated using a Root Mean Square (RMS) metric. To specifically capture the behavior of the wave close to the final time and respect the natural energy norm, this metric is evaluated over a tailored simulation time window $[T - m\Delta t, T]$, with $m \in \mathbb{N}$. Because the involved quantities are defined continuously inside each timeslab, the RMS of the spatial $L^2(\Omega)$ norm is computed by numerically integrating the continuous error field $e(\cdot, t)$ via a composite Simpson's 1/3 quadrature rule. Over the m discrete timeslabs $[t_k, t_{k+1}]$, this metric is strictly evaluated by applying the Simpson quadrature rule to the RMS expression defined in (33), i.e.:

$$\mathrm{RMS}_t(\|e\|_{L^2(\Omega)}) = \left(\frac{1}{m\Delta t} \sum_{k=N_t-m}^{N_t-1} \frac{\Delta t}{6} \left(\|e(\cdot, t_k)\|_{L^2(\Omega)}^2 + 4\|e(\cdot, t_{k+1/2})\|_{L^2(\Omega)}^2 + \|e(\cdot, t_{k+1})\|_{L^2(\Omega)}^2 \right) \right)^{1/2} \tag{43}$$

where N_t is the total number of simulated time steps, and $t_{k+1/2} = \frac{t_k + t_{k+1}}{2}$ represents the temporal midpoint of the given timeslab.
Through the upcoming test cases, the performance of the recovery-based framework is analyzed by explicitly tracking and plotting three fundamental quantities for both the spatial and temporal domains. For spatial gradient analysis, we consider the following:

- The *exact spatial error* (red line in the plots): measuring the distance between the exact gradient and the numerical gradient, $\|\nabla u - \nabla u_h\|_{L^2(\Omega)}$.
- The *spatial error estimator* η_{grad} (green line in the plots): evaluating the distance between the recovered continuous gradient and the numerical gradient, $\|G_h u_h - \nabla u_h\|_{L^2(\Omega)}$.
- The *superconvergent recovery error* (blue line in the plots): measuring the distance between the exact gradient and the recovered gradient, $\|\nabla u - G_h u_h\|_{L^2(\Omega)}$.

Similarly, to validate the temporal recovery strategy outlined in Section 3.6, the temporal derivative analysis tracks:

- The *exact temporal error* (red line in the plots): measuring the exact time derivative against the piecewise constant backward finite difference quotient extracted from the Crank-Nicolson snapshots, $\|\partial_t u - \partial_t u_{h,\Delta t}\|_{L^2(\Omega)}$.

- The *temporal error estimator* η_{time} (green line in the plots): comparing the continuous recovered time derivative to the algebraic difference quotient, $\|G_{\Delta t} u_{h,\Delta t} - \partial_t u_{h,\Delta t}\|_{L^2(\Omega)}$.
- The *superconvergent temporal recovery error* (blue line in the plots): measuring how well the recovered temporal derivative approximates the true analytical time derivative, $\|\partial_t u - G_{\Delta t} u_{h,\Delta t}\|_{L^2(\Omega)}$.

By comparing these respective quantities under uniform spatial and temporal refinements, we will compute the corresponding effectivity indices and observe the asymptotic exactness of the proposed estimators in the hyperbolic regime.

4.1. Test Case 1: 1D Acoustic Wave Equation - Regular Sinusoidal Wave

Our starting point is the one-dimensional acoustic wave equation, as described in (1) with $d = 1$. We consider the setting of the D'Alembert solution of the acoustic wave equation on an unbounded domain $\Omega \equiv \mathbb{R}$, considering a fixed wave speed $c(x) \equiv 1\ \forall x \in \Omega$, by imposing $\eta(x) = \gamma(x) = 1\ \forall x \in \Omega$ and considering no source term $f(x,t) \equiv 0\ \forall (x,t) \in \Omega \times (0,T]$. Choosing a null initial velocity $v_0(x) = 0\ \forall x \in \Omega$ and an initial displacement $u_0(x)$, the exact stationary solution of this model problem can be analytically derived:

$$u(x,t) = \frac{1}{2}[u_0(x+t) + u_0(x-t)] \tag{44}$$

This holds on the whole unbounded domain $\mathbb{R}$, but numerically, we can only work on a finite bounded domain $\Omega = [0,1]$. Therefore, to guarantee the analytical solution to resemble the numerical one, we need to impose boundary conditions like $u(0,t) = u(1,t) = 0\ \forall t \in [0,T]$. Hence, if we impose a null initial velocity, and an initial signal $\varphi(x)$ satisfying the boundary conditions described before, i.e. $\varphi(0) = \varphi(1) = 0$, we ensure that the odd- and 2- periodic extension $u_0(x)$ of the initial signal $\varphi(x)$ automatically satisfies the null boundary conditions imposed by the problem.
In this test case, we chose a sinusoidal initial displacement, so $\varphi(x) = \sin(\pi x), x \in [0,1]$; in this way, the odd-2-periodic displacement coincides exactly with the sinusoidal function on the full domain, i.e. $u_0(x) = \varphi(x)\ \forall x \in \Omega$. The simulation has been performed by using a final time $T = 1$, with an RMS-time window of $m = 10$ timeslabs. The discretization mesh sizes considered for this test are $h = \{\frac{1}{2^4}, \frac{1}{2^5}, \frac{1}{2^6}, \frac{1}{2^7}\}$. Lastly, as already specified at the end of Section 2, to guarantee the correct balance between temporal and spatial error contributions, we set the temporal step size equal to the spatial mesh size, so at each iteration, we have $\Delta t = h$.

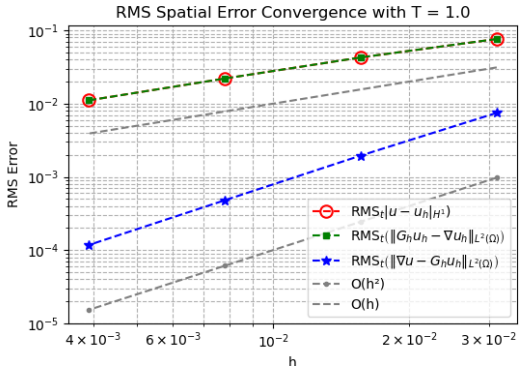

(a) Convergence rates for the spatial error on the 1D Sinusoidal Solution of the Acoustic Wave Equation.

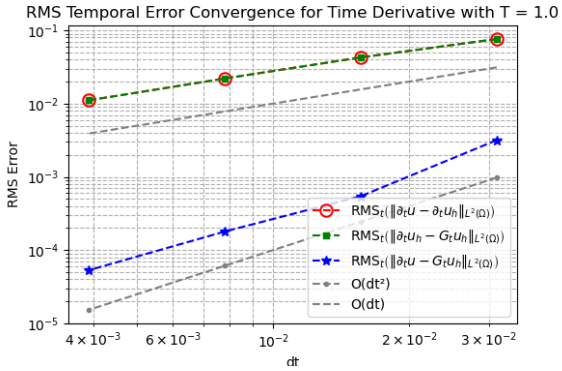

(b) Convergence rates for the temporal error on the 1D Sinusoidal Solution of the Acoustic Wave Equation.

Figure 4: Exact errors (red), *a-posteriori* error estimators (green) and superconvergent errors (blue) for the 1D Sinusolidal Solution of the Acoustic Wave Equation.

Figure 4 shows the log-log plots of the spatial and temporal errors measured in their RMS-time norm along the various mesh sizes h and temporal step sizes Δt, together with the expected theoretical orders of convergence. As one can notice from the left plot in Figure 4a, the spatial recovery-based error estimator (in green) converges to the exact H^1-seminorm of the true error (in red), with the same order $\mathcal{O}(h)$, as we are using Finite Element solutions with piecewise linear polynomials. This happens thanks to the superconvergent quantity $\|\nabla u - G_h u_h\|_{L^2(\Omega)}$, which gains one order of convergence, aligning these results with the theoretical expectations. An analogous reasoning extends to the analysis of the temporal discretization errors, as depicted in Figure 4b. The results demonstrate that the temporal recovery-based error estimator successfully converges to the true temporal error, with both quantities exhibiting a strict linear convergence rate of $\mathcal{O}(\Delta t)$. This reduction to first-order accuracy is fundamentally consistent with the underlying time-stepping scheme: while the Crank-Nicolson method yields a second-order accurate primal solution, the numerical evaluation of its temporal derivative intrinsically sacrifices one order of convergence.
Our analysis extends also to the performance of the error estimators in terms of their asymptotic exactness, by computing the effectivity index for each discretization step. Table 1 shows, for both the spatial and temporal error indicators, that the effectivity index computed as:

$$\text{Eff. Index} = \frac{\text{RMS}_{\text{rec}}}{\text{RMS}_{\text{classic}}}$$

tends to 1 as the discretization steps tends to 0, proving numerically their asymptotical exactness.

Table 1: Global RMS errors and effectivity indices for the 1D Sinusoidal SOlution of the Acoustic Wave Equation.

(a) Spatial RMS Errors

h	$\text{RMS}_{\text{classic}}$	RMS_{rec}	RMS_{sup}	Eff. Index
$1/2^4$	7.63064×10^{-2}	7.64000×10^{-2}	7.48938×10^{-3}	1.0012
$1/2^5$	4.27707×10^{-2}	4.27874×10^{-2}	1.95380×10^{-3}	1.0004
$1/2^6$	2.20355×10^{-2}	2.20378×10^{-2}	4.79154×10^{-4}	1.0001
$1/2^7$	1.11013×10^{-2}	1.11016×10^{-2}	1.17324×10^{-4}	1.0000

(b) Temporal RMS Errors

Δt	$\text{RMS}_{t,\text{classic}}$	$\text{RMS}_{t,\text{rec}}$	$\text{RMS}_{t,\text{sup}}$	Eff. Index
$1/2^4$	7.63233×10^{-2}	7.61324×10^{-2}	3.17592×10^{-3}	0.9975
$1/2^5$	4.27791×10^{-2}	4.27436×10^{-2}	5.44021×10^{-4}	0.9992
$1/2^6$	2.20368×10^{-2}	2.20320×10^{-2}	1.79161×10^{-4}	0.9998
$1/2^7$	1.11015×10^{-2}	1.11009×10^{-2}	5.31070×10^{-5}	0.9999

4.2. Test Case 2: 1D Acoustic Wave Equation - Solution with Steeper Gradients

While the first test case focused on a smooth, low-frequency analytical solution, this second test evaluates the estimators against a solution with significantly steeper gradients. This is a necessary step because hyperbolic equations, unlike elliptic ones, do not regularize the solution. Instead, they preserve the exact regularity of the initial data, meaning that any sharp wave front will simply propagate along the domain characteristics without physical attenuation. In terms of the recovery-based theory, the error indicators conceptualized in this work might experience either spurious oscillations or being late in approximating the actual spatial or temporal derivative. This behavior will not allow them to get the required superconvergence and make the estimators effectively work, as assumptions of regularity of the exact solution are required in the theory to make the estimates hold.

To evaluate the estimators against localized variations, this test manufactures a 1D D'Alembert solution following the general setting of the previous section. However, the profile is now constructed explicitly by defining the spatial gradient of the initial condition $\varphi(x)$:

$$\frac{d\varphi}{dx}(x) = \sigma\left(\frac{x-a}{\epsilon}\right) - \sigma\left(\frac{x-b}{\epsilon}\right) \quad \forall x \in \Omega = [0,1],$$

where $\sigma(z) = \frac{1}{1+e^{-z}}$ is the standard sigmoid function, which provides a smooth but rapid transition centered at $z = 0$. The parameters $a = 0.25$ and $b = 0.75$ position the two wave fronts within the domain, while $\epsilon = 0.01$ acts as a scaling factor that dictates their sharpness. By adjusting ϵ, we strictly control the steepness of the gradient; as $\epsilon \to 0$, the transition becomes increasingly abrupt, approaching a localized discontinuity. By integrating in space on the interval $\Omega = [0,1]$, we get:

$$\varphi(x) = \epsilon\left(\log\left(1 + e^{\frac{x-a}{\epsilon}}\right) - \log\left(1 + e^{\frac{x-b}{\epsilon}}\right)\right) \tag{45}$$

Now, we just need to enforce the condition $\varphi(0) = \varphi(1) = 0$ in order to guarantee our initial data to be continuous over its odd-2-periodic extension $u_0(x)$. Therefore, we add a linear correction:

$$\hat{\varphi}(x) = \varphi(x) - ((1-x)\varphi(0) + x\varphi(1)) \tag{46}$$

so that $\hat{\varphi}(0) = \hat{\varphi}(1) = 0$. Then, as done for the setting of the sinusoidal test case, we impose a homogeneous initial velocity field, $v_0(x) = 0$. Consequently, following the classical D'Alembert formulation for the 1D acoustic wave equation, the exact analytical solution at any arbitrary time t is strictly governed by the translation of the initial displacement profile. By denoting $u_0(x)$ as the odd, 2-periodic extension of our corrected initial data $\hat{\varphi}(x)$ over the entire real line, the exact dynamic solution is evaluated as done in (44). This formulation ensures that the two sharp wave fronts initialized symmetrically around $a = 0.25$ and $b = 0.75$ will split and travel continuously across the domain. The numerical simulation is carried out with a unitary wave speed $c = 1$ up to a final simulation time $T = 1$. Since the numerical discretization of FEM with piecewise linear polynomials in space and Crank-Nicolson in time should solve steeper solutions, a finer set of mesh discretization steps is considered, namely $h = \{\frac{1}{2^7}, \frac{1}{2^8}, \frac{1}{2^9}, \frac{1}{2^{10}}, \frac{1}{2^{11}}\}$, and the temporal step size Δt is chosen to be equal to the step size h. The RMS will then be computed considering $m = 30$ timeslabs, since we are using much smaller time refinements.

For the case of steep gradients, as shown in Figure 5, coarse meshes exhibits pre-asymptotic behavior due to the under resolution of the transitional steep layer of the wave signal, both in space and time. As the asymptotic regime is met, the convergence rates are restored and the error indicator converges to the true error both in space, as seen in Figure 5a, and time, as one can observe in Figure 5b, coherently with the theoretical expectations. Furthermore, Table 2 shows that the error indicators are both asymptotically exact, as their effectivity index converges to 1, as we refine both spatial and temporal discretization refinements parameters $h, \Delta t$.

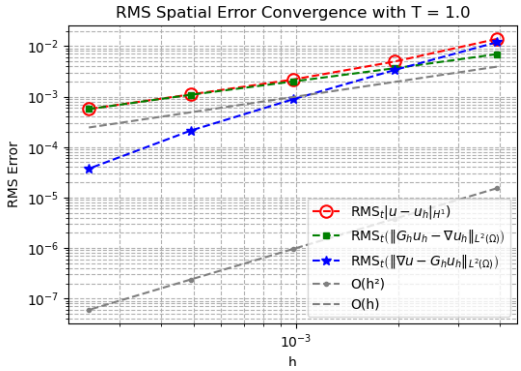

(a) Convergence rates for the spatial error on the 1D Steeper Solution of the Acoustic Wave Equation.

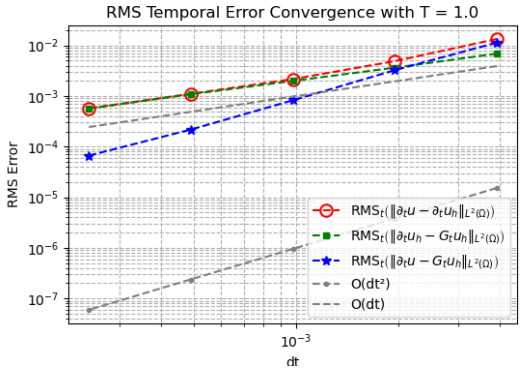

(b) Convergence rates for the temporal error on the 1D Steeper Solution of the Acoustic Wave Equation.

Figure 5: Exact errors (red), *a-posteriori* error estimators (green) and superconvergent errors (blue) for the 1D Steeper Solution of the Acoustic Wave Equation.

Table 2: Global RMS errors and effectivity indices for the 1D Acoustic Wave Equation with steep gradients (D'Alembert solution).

(a) Spatial RMS Errors

h	$\mathrm{RMS}_{\mathrm{classic}}$	$\mathrm{RMS}_{\mathrm{rec}}$	$\mathrm{RMS}_{\mathrm{sup}}$	Eff. Index
$1/2^8$	1.38315×10^{-2}	6.91780×10^{-3}	1.19002×10^{-2}	0.5001
$1/2^9$	4.94952×10^{-3}	3.64409×10^{-3}	3.36491×10^{-3}	0.7363
$1/2^{10}$	2.17163×10^{-3}	1.99020×10^{-3}	8.80934×10^{-4}	0.9165
$1/2^{11}$	1.10516×10^{-3}	1.08584×10^{-3}	2.12342×10^{-4}	0.9825
$1/2^{12}$	5.66831×10^{-4}	5.65756×10^{-4}	3.73046×10^{-5}	0.9981

(b) Temporal RMS Errors

Δt	$\mathrm{RMS}_{t,\mathrm{classic}}$	$\mathrm{RMS}_{t,\mathrm{rec}}$	$\mathrm{RMS}_{t,\mathrm{sup}}$	Eff. Index
$1/2^8$	1.34216×10^{-2}	6.88240×10^{-3}	1.14011×10^{-2}	0.5128
$1/2^9$	4.89701×10^{-3}	3.63990×10^{-3}	3.24727×10^{-3}	0.7433
$1/2^{10}$	2.16007×10^{-3}	1.98965×10^{-3}	8.23698×10^{-4}	0.9211
$1/2^{11}$	1.10933×10^{-3}	1.08572×10^{-3}	2.17606×10^{-4}	0.9787
$1/2^{12}$	5.69885×10^{-4}	5.65732×10^{-4}	6.66002×10^{-5}	0.9927

4.3. Test Case 3: 2D Acoustic Wave Equation - Regular Sinusoidal Solution

The purpose of the next two test cases is to analyze the performance of the recovery-based error estimators in space and time for the numerical solution of the two-dimensional acoustic wave equation. It is worth specifying that the analytical D'Alembert solutions, which can be taken into account for the 1D numerical tests, can not be directly extended to higher dimensions. Therefore, in this test case, we will proceed with the Method of Manufactured Solutions (MMS), and establish an exact solution to the strong problem (1). Having validated the estimators on the one-dimensional configurations, this third test case extends the numerical experiments to a two-dimensional spatial domain $\Omega = [0,1] \times [0,1]$. The spatial discretization is performed over a sequence of uniformly refined structured quadrilateral meshes $\mathcal{Q}_h$, characterized by the spatial step size $h \in \{\frac{1}{2^4}, \frac{1}{2^5}, \frac{1}{2^6}, \frac{1}{2^7}\}$, while the dynamic evolution is integrated up to a final simulation time $T = 2.0$ using a uniform temporal step $\Delta t = h$. To properly assess the performance of the estimators, we manufacture a smooth 2D analytical solution, specifically a standing wave profile defined as $u(x, y, t) = \sin(\pi x)\sin(\pi y)\cos(\sqrt{2}\pi t)$, assuming a unitary wave speed $c = 1$. As detailed in the introduction of this chapter, all the error quantities are evaluated using the continuous RMS metric computed over a specifically condensed simulation time window $[T - m\Delta t, T]$ with $m = 10$, to effectively capture the asymptotic dynamics without being biased by specific zero-crossing instances of the oscillatory wave. From a theoretical standpoint, the choice of such a highly regular and smooth analytical solution also in 2D is strictly necessary to place our numerical experiment perfectly within the optimal framework required by the superconvergence theory.

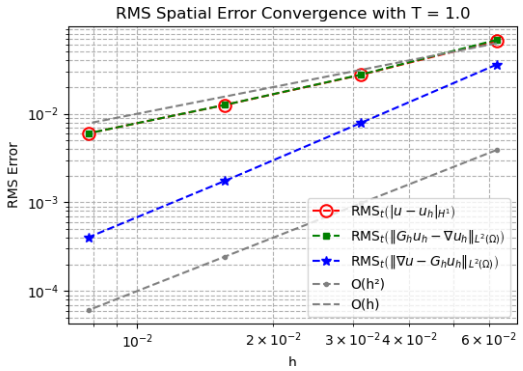

(a) Convergence rates for the spatial error on the 2D Sinusoidal Solution of the Acoustic Wave Equation.

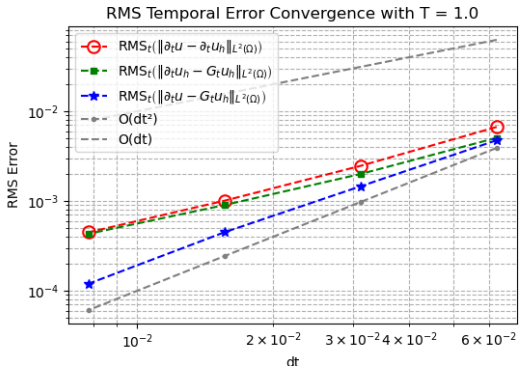

(b) Convergence rates for the temporal error on the 2D Sinusoidal Solution of the Acoustic Wave Equation.

Figure 6: Exact errors (red), *a-posteriori* error estimators (green) and superconvergent errors (blue) for the 2D Sinusoidal Solution of the Acoustic Wave Equation.

Table 3: Global RMS errors and effectivity indices for the 2D Standing Wave analytical solution.

(a) Spatial RMS Errors

h	$\text{RMS}_{\text{classic}}$	RMS_{rec}	RMS_{sup}	Eff. Index
$1/2^4$	6.66061×10^{-2}	6.82655×10^{-2}	3.59180×10^{-2}	1.0249
$1/2^5$	2.74378×10^{-2}	2.76083×10^{-2}	7.87771×10^{-3}	1.0062
$1/2^6$	1.25584×10^{-2}	1.25851×10^{-2}	1.74602×10^{-3}	1.0021
$1/2^7$	6.02495×10^{-3}	6.02862×10^{-3}	4.05077×10^{-4}	1.0006

(b) Temporal RMS Errors

Δt	$\text{RMS}_{t,\text{classic}}$	$\text{RMS}_{t,\text{rec}}$	$\text{RMS}_{t,\text{sup}}$	Eff. Index
$1/2^4$	6.69401×10^{-3}	5.06561×10^{-3}	4.75661×10^{-3}	0.7567
$1/2^5$	2.46829×10^{-3}	2.00172×10^{-3}	1.46097×10^{-3}	0.8110
$1/2^6$	1.01044×10^{-3}	9.02682×10^{-4}	4.50053×10^{-4}	0.8934
$1/2^7$	4.48774×10^{-4}	4.31970×10^{-4}	1.20117×10^{-4}	0.9626

As noted in Figure 6a and Table 3a, one can observe that the RMS-in-time of the recovery-based spatial error estimator η_{grad} (in green) follows the same order of the exact error (in red), actually overlapping. The overlapping is also confirmed by the results in Table 3a, where we notice that the Effectivity index goes to 1.0006 on the last mesh refinement, supporting the asymptotic exactness of the error indicator. Analogously, the temporal recovery-based error estimator follows the convergence rate of the exact temporal error, thanks to the superconvergent temporal recovery error, which gains order $O(\Delta t^2)$, leading to confirm the theoretical assumptions. As shown in Table 3b, we can notice that here the effectivity

index starts a bit lower (0.7567 for the coarsest mesh), but as long as we refine $\Delta t \to 0$, the error estimator gets closer to the exact error. Evaluating the global RMS norms over the entire domain is strictly necessary to assess the asymptotic

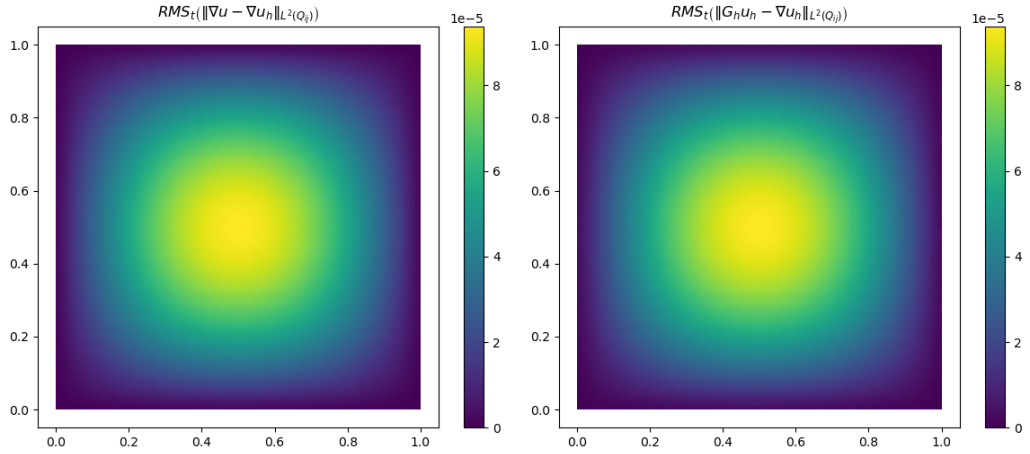

(a) Element-wise distribution of the spatial error indicator ($\eta^2_{K,grad}$) for the 2D Sinusoidal Solution of the Acoustic Wave Equation: on the left, the RMS-in-time of the exact error; on the right, the RMS-in-time of the recovery-based error indicator.

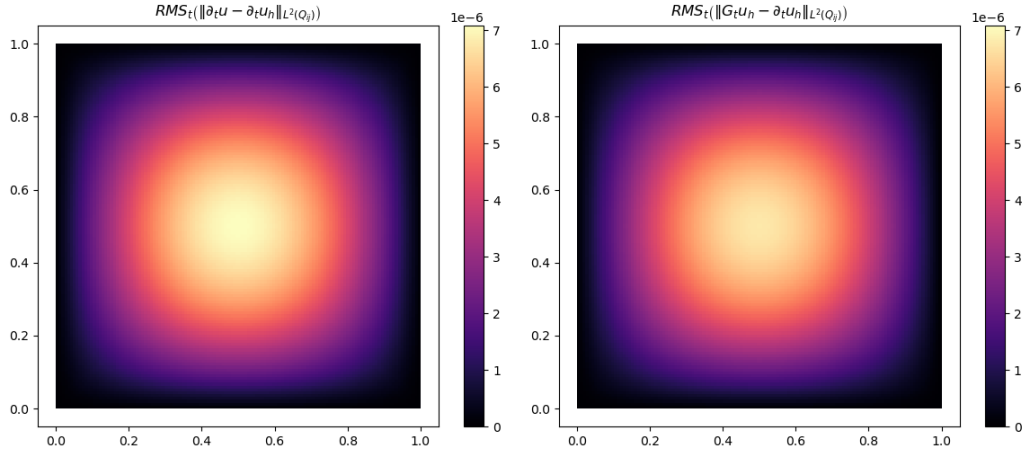

(b) Element-wise distribution of the temporal error indicator for the 2D Sinusoidal Solution of the Acoustic Wave Equation: on the left, the RMS-in-time of the exact error; on the right, the RMS-in-time of the recovery-based error indicator.

Figure 7: Localized distribution of the recovery-based spatial and temporal error indicators evaluated on the finite element mesh for the 2D Sinusoidal Solution of the Acoustic Wave Equation.

convergence rates, but it hides how the error is distributed. To better investigate the reliability of the recovery operators, we computed the local distribution of the RMS errors element by element. More specifically, for the spatial error plot shown in Figure 7a, we calculate the square of the local error estimator strictly inside each element $K \in \mathcal{Q}_h$ as:

$$\eta^2_{K,grad} = \int_K |G_h u_h - \nabla u_h|^2 dx \tag{47}$$

To effectively plot these quantities in our FEniCSx implementation, we defined a Discontinuous Galerkin function space of degree zero (DG_0). Since a DG_0 space associates exactly one degree of freedom to the center of each cell, we evaluated the integral of the squared error cell by cell and assigned this constant value to the corresponding degree of freedom. The same reasoning is applied to the temporal derivative in Figure 7b, where we integrate the difference $|G_{\Delta t} u_{h,\Delta t} - \partial_t u_{h,\Delta t}|^2$ over the elements. After that, as done for the global case, all the errors are averaged according to the RMS-in-time technique used in (43).As it is possible to see from the heatmaps, the distribution of our error indicator is practically identical to the distribution of the true exact error. This visually confirms that the recovery strategy not only matches the exact error globally with an effectivity index close to 1, but it also successfully tracks the areas of the mesh where the highest approximation errors are located, opening the door for future adaptive mesh refinement strategies.

4.4. Test Case 4: 2D Acoustic Wave Equation - Gaussian Pulse with Steep Gradients

Following the validation on a highly regular analytical solution, this final test case evaluates the performance of the recovery-based error estimators under significantly more demanding dynamic conditions in two dimensions. Similar to the analysis conducted in Section 4.2, we move away from smooth profiles and manufacture a solution characterized by severe localized variations. Specifically, the domain $\Omega = [0,1] \times [0,1]$ is initialized with a sharp Gaussian pulse centered at $(0.5, 0.5)$, defined by the initial displacement $u_0(x,y) = e^{-((x-0.5)^2+(y-0.5)^2)/\epsilon}$. The steepness parameter is set to a highly restrictive value of $\epsilon = 0.005$. The problem is configured with a zero source term ($f = 0$) and homogeneous Dirichlet boundary conditions ($u = 0$ on $\partial\Omega$). From a strictly analytical standpoint, a Gaussian profile never perfectly vanishes at a finite distance; however, with $\epsilon = 0.005$, the displacement evaluated at the boundaries is on the order of e^{-50}. This discrepancy creates a theoretical gap at the domain edges, but it is numerically negligible and strictly compatible with the imposed zero boundary conditions without introducing spurious corner singularities. The physical evolution of this configuration is particularly challenging for a-posteriori error estimation. As the simulation evolves, the steep radial pulse expands outward, collides against the fixed walls of the domain, and reflects back towards the center. This reflection mechanism generates complex wave interferences, sharp numerical wiggles, and high-frequency oscillatory patterns trailing the main wavefront. Consequently, the primary objective of this test is to verify whether the spatial and temporal recovery operators, G_h and $G_{\Delta t}$, are robust enough to accurately perceive and track these propagating oscillations once the wave has been heavily distorted by the boundary impacts.
The numerical simulation is carried out up to a final time $T = 1.0$. The spatial discretization employs a sequence of structured quadrilateral meshes $\mathcal{Q}_h$, with sizes $h \in \{\frac{1}{2^4}, \frac{1}{2^5}, \frac{1}{2^6}, \frac{1}{2^7}, \frac{1}{2^8}, \frac{1}{2^9}\}$. To maintain the fundamental balance between spatial and temporal truncation errors, the Crank-Nicolson time step is kept strictly coupled to the spatial grid, ensuring $\Delta t = h$. The errors are then computed using the same RMS-in-time technique considering the last $m = 30$ timeslabs in the localized temporal interval $[T - m\Delta t, T]$. Furthermore, since this setting does not provide us with an analytical exact solution, a numerical reference solution $u_{h_{ref}}$ is computed on a reference finer mesh with discretization parameter $h_{ref} = \frac{1}{2^{11}}$, and considering the corresponding time step $\Delta t_{ref} = h_{ref}$.

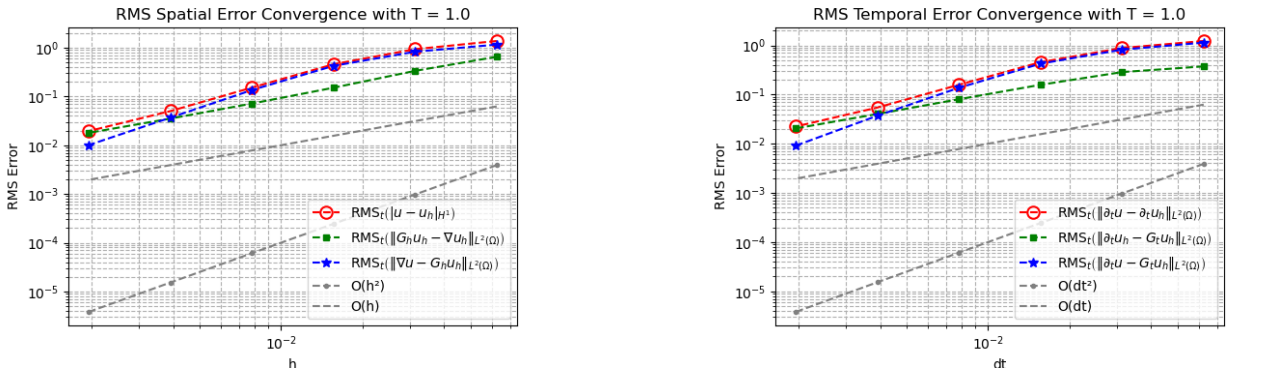

(a) Convergence rates for the spatial error on the 2D Gaussian Pulse Solution of the Acoustic Wave Equation.

(b) Convergence rates for the temporal error on the 2D Gaussian Pulse Solution of the Acoustic Wave Equation.

Figure 8: Exact errors (red), *a-posteriori* error estimators (green) and superconvergent errors (blue) for the 2D Gaussian Pulse Solution of the Acoustic Wave Equation.

As one can notice in Figure 8 and Table 4, the recovered quantities in the RMS-in-time natural norm exhibits superconvergence only when considering the finest meshes, leaving the majority of the coarser meshes to show only the pre-asymptotic regime. This happens because the underlying exact solution is characterized by high-frequency wiggles and oscillations, therefore it violates the assumption of regularity needed for the superconvergence to happen. However, for the last refinement step, one can still notice the recovery-based error indicators in space and time to converge to the actual error between the numerical solution against the reference one, as also supported by the spatial and temporal effectivity indices in Tables 4a, 4b.
Figures 9a, 9b show the comparison (both in space and time) between the RMS-in-time of the actual error (on the left) and the RMS-in-time of the error indicator, visualized for the last mesh refinement $h = \frac{1}{2^9}$. As one can observe, the error indicators locally identify the features of the error due to both the space and time variables, even if the initial Gaussian smooth pulse propagates in time in a bounded domain, letting the high-frequency wiggles overcome the low-frequency ones and increasing the steepness of the gradients over time.

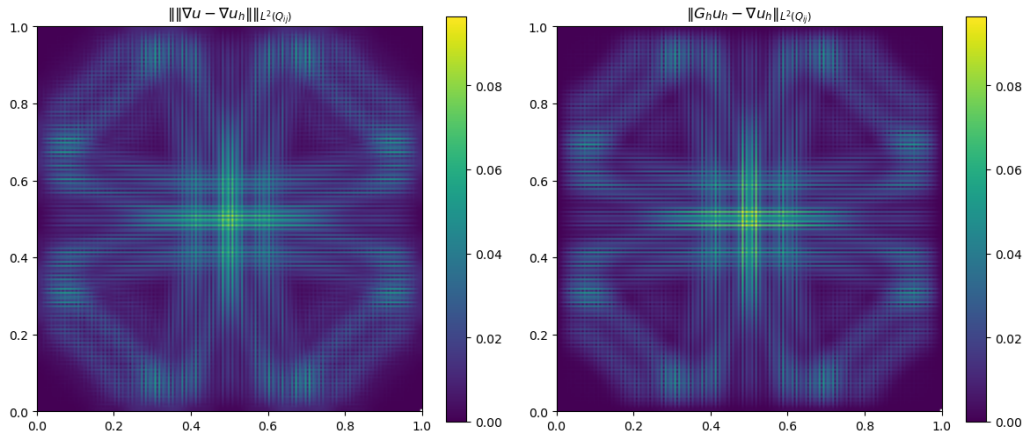

(a) Element-wise distribution of the spatial error indicator ($\eta^2_{K,grad}$) for the 2D Gaussian Pulse Solution of the Acoustic Wave Equation: on the left, the RMS-in-time of the exact error; on the right, the RMS-in-time of the recovery-based error indicator.

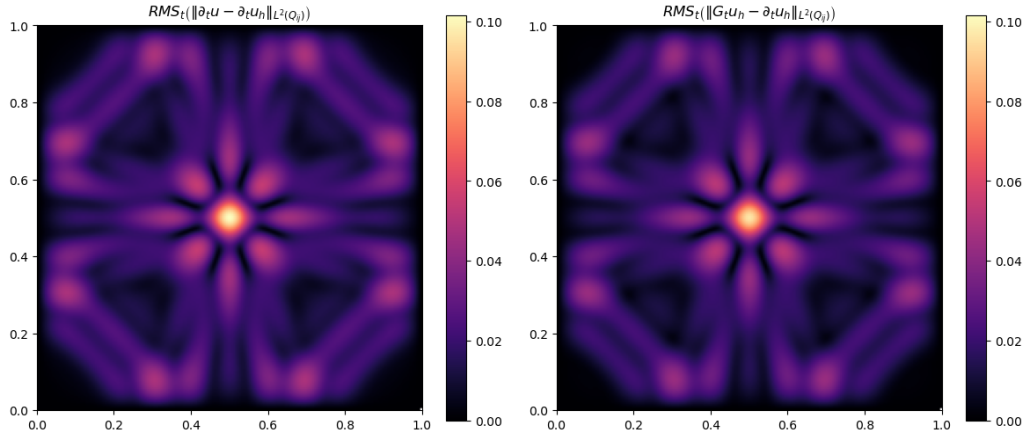

(b) Element-wise distribution of the temporal error indicator for the 2D Gaussian Pulse Solution of the Acoustic Wave Equation: on the left, the RMS-in-time of the exact error; on the right, the RMS-in-time of the recovery-based error indicator.

Figure 9: Localized distribution of the recovery-based spatial and temporal error indicators evaluated on the finite element mesh for the 2D Gaussian Pulse Solution of the Acoustic Wave Equation.

Table 4: Global RMS errors and effectivity indices for the 2D Gaussian Pulse Wave solution.

(a) Spatial RMS Errors

h	$\mathrm{RMS}_{\mathrm{classic}}$	$\mathrm{RMS}_{\mathrm{rec}}$	$\mathrm{RMS}_{\mathrm{sup}}$	Eff. Index
$1/2^4$	1.37344×10^{0}	6.51905×10^{-1}	1.15704×10^{0}	0.4747
$1/2^5$	9.32888×10^{-1}	3.34994×10^{-1}	8.27107×10^{-1}	0.3591
$1/2^6$	4.58111×10^{-1}	1.51140×10^{-1}	4.24621×10^{-1}	0.3299
$1/2^7$	1.52162×10^{-1}	7.15185×10^{-2}	1.35458×10^{-1}	0.4700
$1/2^8$	5.01015×10^{-2}	3.51712×10^{-2}	3.67614×10^{-2}	0.7020
$1/2^9$	1.95059×10^{-2}	1.79580×10^{-2}	1.00712×10^{-2}	0.9206

(b) Temporal RMS Errors

Δt	$\mathrm{RMS}_{t,\mathrm{classic}}$	$\mathrm{RMS}_{t,\mathrm{rec}}$	$\mathrm{RMS}_{t,\mathrm{sup}}$	Eff. Index
$1/2^4$	1.22746×10^{0}	3.73927×10^{-1}	1.13746×10^{0}	0.3046
$1/2^5$	8.83862×10^{-1}	2.86235×10^{-1}	8.19337×10^{-1}	0.3238
$1/2^6$	4.55175×10^{-1}	1.57820×10^{-1}	4.24561×10^{-1}	0.3467
$1/2^7$	1.58167×10^{-1}	8.02898×10^{-2}	1.37350×10^{-1}	0.5076
$1/2^8$	5.44145×10^{-2}	4.02336×10^{-2}	3.70729×10^{-2}	0.7394
$1/2^9$	2.24307×10^{-2}	2.05242×10^{-2}	9.13926×10^{-3}	0.9150

5. Alfvén Waves: description and numerical results of recovery-based indicators

In this section, recovery-based spatial and temporal error estimators are analyzed for plasma physics, namely on the shear electrostatic Alfvén wave equations. Before describing the numerical experiments, we give a brief explanation of plasma physics, the hyperbolic model problem and its discretization in space and time. Then, numerical convergence tests are presented to analyze the performance of the spatial and temporal recovery-based error estimators on this specific problem, and, finally, an adaptive mesh refinement strategy is implemented and described.

5.1. Shear Electrostatic Alfvén Waves: Background and Mathematical Model

Nowadays, the mathematical modeling of plasma turbulence constitutes a fundamental challenge in the development of magnetic confinement fusion devices. A plasma is traditionally defined as a highly ionized gas that, while remaining macroscopically neutral, exhibits strong collective interactions dominated by long-range electromagnetic forces rather than localized, binary collisions [13]. Because of these collective behaviors, fully describing a plasma requires kinetic theory, which models the statistical distribution of particles in a six-dimensional phase space. While kinetic models provide the most physically comprehensive description of plasma dynamics, they are computationally expensive for simulating macroscopic phenomena over extended spatial and temporal scales [12].

To avoid the computational bottlenecks inherent to kinetic theory, it is standard practice to conceptualize the plasma as a continuum. By taking velocity moments of the underlying kinetic equations, the system can be rigorously reduced to macroscopic fluid models [17]. The most widely utilized framework in this context is Magnetohydrodynamics (MHD), which treats the plasma as a single, electrically conducting fluid coupled to Maxwell's equations. Ideal MHD successfully captures large-scale, low-frequency macroscopic instabilities, but shows strong limitations to describe small-scale turbulence, particularly in regions characterized by steep pressure gradients and strong magnetic fields. This limitation is especially critical when modeling the boundary region of the plasma, commonly referred to as the scrape-off layer (SOL).

To effectively simulate these highly turbulent, strongly magnetized regimes, the continuous physical phenomena are generally described using the drift-reduced Braginskii equations [23, 28]. This advanced fluid model accounts for finite Larmor radius effects and separates the fast particle motion along the magnetic field lines from the slower, perpendicular drift velocities (specifically, the $E \times B$ and diamagnetic drifts). Although the Braginskii model that reduces drift provides a robust mathematical foundation for large-scale computational analysis of the SOL, it remains a highly complex, nonlinear, and coupled system of partial differential equations.

Within this framework, different physical phenomena evolve across vastly different time scales. Notably, the fastest oscillatory dynamics are captured by the shear electrostatic Alfvén waves. Because these waves propagate along the magnetic field lines at extremely high speeds relative to the perpendicular turbulent transport, they impose the most severe stability constraints on explicit temporal integration schemes [15, 24]. Consequently, isolating and accurately resolving this specific high-frequency hyperbolic subsystem is a foundational step toward developing robust, unconditionally stable numerical methods for the complete macroscopic plasma model.

In this work, we start by describing the mathematical framework to define the model for the shear electrostatic Alfvén

waves. We follow the theoretical description done in [6], where numerical simulations are done in a 3D *tokamak*, a torus-shaped chamber with a rectangular cross section, which is described as:

$$\mathbb{T} = \{(x, y, z) \in \mathbb{R}^3 : r_{in}^2 < x^2 + y^2 < r_{out}^2, 0 < z < z_{max}\} \tag{48}$$

with $r_{min} > 0, r_{max} > 0$ being the inner and outer radius of the torus and $z_{max} > 0$ being the height. However, in this section, we will limit the analysis to a 2D projection of the *tokamak* domain on the $xy-$plane, obtaining an annulus-shaped region defined as:

$$\Omega := \mathbb{T}_2 = \{(x, y) \in \mathbb{R}^2 : r_{in}^2 < x^2 + y^2 < r_{out}^2\} \tag{49}$$

Then, let $U \subset \mathbb{R}^2$ be an open set such that $\bar{\Omega} \subset U$. We then define the magnetic vector field $\vec{B} : U \to \mathbb{R}^2$, such that it is divergence-free, namely $\nabla \cdot \vec{B} = 0$, and its corresponding normalization $\vec{b} = \frac{\vec{B}}{\|\vec{B}\|}$. Furthermore, it is assumed that $\vec{b} \in C^1(U, \mathbb{R}^2)$ and that $\forall x \in U$, $\exists \vec{k} \in \mathbb{R}^2$ such that $\vec{b}(x) \cdot \vec{k} > 0$, i.e. the magnetic normalized field has a global direction. In the case of our domain being an annulus-shaped region, the magnetic field is oriented towards the azimuthal direction, i.ie, it will follow the circumference of the anular region.
Then, we define $u, \phi : \Omega \times [0, T] \to \mathbb{R}$ as respectively the component of the electron velocity parallel to the magnetic field $\vec{b}$, and the electrostatic potential. Since the magnetic field is leading the direction of the movement of plasma when considering the shear electrostatic Alfvén waves, it is good practice in this setting to define the perpendicular gradient as:

$$\nabla_\perp \phi := \nabla\phi - \vec{b}(\vec{b} \cdot \nabla\phi) = (I - \vec{b}\vec{b}^T)\nabla\phi \tag{50}$$

This corresponds to the projection of the gradient of the electrostatic potential ϕ on the orthogonal complement of the magnetic field $\vec{b}$. The strong form of the mathematical model for the shear electrostatic Alfvén waves reads:

$$\begin{cases} \mu \frac{\partial u}{\partial t}(x,t) - \vec{b}(x) \cdot \nabla\phi(x,t) = f(x,t) & x \in \Omega, t \in (0,T], \\ \frac{\partial}{\partial t}\text{div}(\nabla_\perp \phi(x,t)) + \text{div}(\vec{b(x)}u(x,t)) = g(x,t) & x \in \Omega, t \in (0,T], \\ \phi(x,t) = 0 & x \in \partial\Omega, t \in (0,T], \\ u(x,0) = u_0(x) & x \in \Omega, \\ \phi(x,0) = \phi_0(x) & x \in \Omega, \end{cases} \tag{51}$$

where $\mu > 0$ is the parameter describing the ratio between the electron and ion mass, f, g on $\Omega \times [0, T]$ represent the source terms, and u_0, ϕ_0 the initial data for the parallel velocity and the potential, respectively. As motivated in the first chapters of this work, it is fundamental for the error analysis to introduce the natural energy norm of the Alfvén waves model (51), which will be then estimated within the RMS strategy (33) by the recovery-based error estimators. The natural energy norm of this problem at final time $t = T$ reads:

$$\mu\|u(\cdot, T)\|^2_{L^2(\Omega)} + \|\nabla_\perp \phi(\cdot, T)\|^2_{L^2(\Omega)} \tag{52}$$

Hereafter, two different discretizations in space and time are presented: the first one applies a standard Finite Element Method as a space discretization on both the equations, combining it with a Crank-Nicolson time-stepping discretization in time; the second one instead, attempts to decouple the problem for the potential $\phi(x, t)$ before performing the spatial FEM and temporal Newmark discretization only on this equation, and then update the velocity $u(x, t)$ accordingly to the equation left out.
Method 1. Here, we propose a weak formulation of both the equations regulating the shear electrostatic Alfvén waves, as done in [6]. First we define an appropriate Sobolev space needed for this formulation.

Definition 1 ($H^1_{\perp,0}$ functional space)**.** *Let $\Omega \subset \mathbb{R}^n$ be an open set, and $\vec{b_1}, ..., \vec{b_n} \in [Lip(\Omega)]^n$ an orthonormal frame, with $\vec{b} := \vec{b_1}$. We define the space $H^1_\perp(\Omega) \subseteq L^2(\Omega)$ as the functional space which contains all the $L^2(\Omega)$ functions which are weakly differentiable along the vector fields $\vec{b_2}, ..., \vec{b_n}$ and whose weak derivatives are $L^2(\Omega)$. Analogously, we can define $H^1_{\vec{b}}(\Omega)$ as the functional space which contains all the $L^2(\Omega)$ functions which are weakly differentiable along $\vec{b}$ and whose weak derivatives are $L^2(\Omega)$. Lastly, $H^1_{\perp,0}$ is the closure of the space of test functions $\mathcal{D}(\Omega)$ with respect to the space $H^1_{\vec{b}}(\Omega)$.*

Then, the weak formulation will look for $u \in H^1(0, T; L^2(\Omega))$ and $\phi \in L^2(0, T; H^1_0(\Omega)) \cap H^1(0, T; H^1_{\perp,0}(\Omega))$ such that for every $v \in L^2(\Omega), \psi \in H^1_0(\Omega)$ and a.e. $t \in [0, T]$, it holds that:

$$\begin{cases} \int_\Omega (\partial_t u(x,t))v(x)dx - \int_\Omega v(x)\vec{b}(x) \cdot \nabla\phi(x,t)dx = \int_\Omega f(x,t)v(x)dx & \forall v \in L^2(\Omega), \\ -\int_\Omega \nabla_\perp(\partial_t\phi(x,t)) \cdot \nabla_\perp\psi(x)dx - \int_\Omega u(x,t)\vec{b}(x) \cdot \nabla\psi(x)dx = \int_\Omega g(x,t)\psi(x)dx & \forall \psi \in H^1_0(\Omega), \end{cases} \tag{53}$$

where $u(\cdot, 0) = u_0$, $\phi(\cdot, 0) = \phi_0$ in $L^2(\Omega)$, with $f \in L^2(0, T; L^2(\Omega))$ and $g \in L^2(0, T; H^{-1}(\Omega))$. To proceed with a spatial FEM discretization, in this case the anular domain Ω is discretized using a triangular mesh $\mathcal{T}_h$ with characteristic mesh size h and a spatial FEM discretization with piecewise quadratic polynomials is performed. The choice of piecewise quadratic polynomials instead of linear ones is supported by Section 3.9, as for the recovery-based error analysis, at least quadratic polynomials are needed to obtain superconvergent nodal points. Hence, we define the FEM space:

$$V_h^2 = \left\{ v_h \in C^0(\bar{\Omega}) \mid v_h|_K \circ F_K \in \mathbb{P}^2(\hat{K}) \quad \forall K \in \mathcal{T}_h,\ v_h|_{\partial\Omega} = 0 \right\} \tag{54}$$

where $\hat{K}$ is the reference 2D triangle and $F_K : \hat{K} \to K$ is the reference affine transformation which maps every point of the reference triangle into the physical element. Unlike the quadrilateral grids used previously, an unstructured triangular mesh natively conforms to curved inner and outer boundaries without requiring complex coordinate transformations. Furthermore, triangles inherently facilitate adaptive mesh refinement (AMR), allowing for highly localized grid resolution with significantly less complexity than quadrilaterals. Assuming $\mathcal{T}_h$ to be shape regular, let N_{dof} be the number of total degrees of freedom associated to the discretized space V_h^2, and let $\{\varphi_j(x,y)\}_{j=1}^{N_{dof}}$ be the corresponding Lagrangian nodal basis functions. The semi-discrete Galerkin approximation looks for solutions $u_h(\cdot,t), \phi_h(\cdot,t)$ for a.e. $t \in (0,T)$ such that they solve (53) $\forall v_h, \psi_h \in V_h^2$. Then, we can write the weak semi-discrete solutions to the Galerkin problem as:

$$u_h(x,y,t) = \sum_{j=1}^{N_{dof}} U_j(t)\varphi_j(x,y) \qquad \phi_h(x,y,t) = \sum_{j=1}^{N_{dof}} \Phi_j(t)\varphi_j(x,y)$$

The final coupled semi-discrete formulation will be as follows:

$$\begin{cases} M\dot{\mathbf{U}}(t) - B\mathbf{\Phi}(t) = \mathbf{F}(t) \\ -A_\perp\dot{\mathbf{\Phi}}(t) - B^T\mathbf{U}(t) = \mathbf{G}(t) \end{cases} \tag{55}$$

where $\mathbf{U}(t) = [U_1(t), \dots, U_{N_{dof}}(t)]^T$ and $\mathbf{\Phi}(t) = [\Phi_1(t), \dots, \Phi_{N_{dof}}(t)]^T$ are the column vectors containing the unknown time-dependent nodal degrees of freedom corresponding to the vector potential and the electrostatic potential, respectively.
The global matrices $M, A_\perp, B \in \mathbb{R}^{N_{dof} \times N_{dof}}$ and the load vectors $\mathbf{F}(t), \mathbf{G}(t) \in \mathbb{R}^{N_{dof}}$ are assembled from their continuous local element-wise contributions. Specifically, M represents the standard global mass matrix, $A_\perp$ is the perpendicular stiffness matrix encoding the transverse Laplacian operator, and B acts as the coupling matrix associated with the parallel gradient derivative $\nabla_\parallel$. Following the standard Galerkin procedure, their entries are defined continuously as:

$$M_{ij} = \int_\Omega \varphi_i(x,y)\varphi_j(x,y)\,dxdy, \quad A_{\perp,ij} = \int_\Omega \nabla_\perp\varphi_i(x,y)\cdot\nabla_\perp\varphi_j(x,y)\,dxdy, \tag{56}$$

$$B_{ij} = \int_\Omega \varphi_i(x,y)\nabla_\parallel\varphi_j(x,y)\,dxdy. \tag{57}$$

Furthermore, the corresponding source vectors are obtained by projecting the continuous right-hand side data of the problem onto the finite element test space:

$$F_i(t) = \int_\Omega f(x,y,t)\varphi_i(x,y)\,dxdy, \quad G_i(t) = \int_\Omega g(x,y,t)\varphi_i(x,y)\,dxdy. \tag{58}$$

As a last step, we apply the Crank-Nicolson scheme for the temporal discretization on the N_t+1 time instants $\{t^n\}_{n=0}^{N_t}$ equispaced with a temporal step size $\Delta t = \frac{T}{N_t}$. Therefore, we get the fully discrete form, which reads:

$$\begin{cases} M\frac{\mathbf{U}^{n+1}-\mathbf{U}^n}{\Delta t} - B\frac{\mathbf{\Phi}^{n+1}+\mathbf{\Phi}^n}{2} = \frac{\mathbf{F}^{n+1}+\mathbf{F}^n}{2} \\ -A_\perp\frac{\mathbf{\Phi}^{n+1}-\mathbf{\Phi}^n}{\Delta t} - B^T\frac{\mathbf{U}^{n+1}+\mathbf{U}^n}{2} = \frac{\mathbf{G}^{n+1}+\mathbf{G}^n}{2} \end{cases} \tag{59}$$

that will be solved at each timestep for $\mathbf{U}^{n+1}, \mathbf{\Phi}^{n+1}$ starting from the discretized initial conditions $\mathbf{U}^0, \mathbf{\Phi}^0$.
Method 2. The second method consists of proceeding firstly with a decoupling of the two equations in (51) and solve the obtained equation for ϕ. We start by deriving in time the second equation, and use the interchange between the divergence operator in space and the temporal derivative, assuming the spatial domain is the same at each time instant:

$$\partial_{tt}\mathrm{div}(\nabla_\perp\phi) + \mathrm{div}(\vec{b}\partial_t u) = \partial_t g \tag{60}$$

Then, we replace the temporal derivative using the first equation in (51), which is $\partial_t u = \frac{1}{\mu}(\vec{b}\cdot\nabla\phi + f)$, and obtain:

$$\partial_{tt}\mathrm{div}(\nabla_\perp\phi) + \frac{1}{\mu}\mathrm{div}(\vec{b}(\vec{b}\cdot\nabla\phi)) = \partial_t g - \frac{1}{\mu}\mathrm{div}(\vec{b}f) \tag{61}$$

By assuming to discretize the domain with the same configuration of Method 1, and use the Finite Element Method on piecewise quadratic polynomial, the corresponding semi-discrete Galerkin formulation of the problem aims to find $\phi_h(\cdot,t) \in V_h^2$ for $t \in (0,T)$, which satisfies:

$$\int_\Omega \nabla_\perp(\partial_{tt}\phi_h)\cdot\nabla_\perp\psi_h dx + \frac{1}{\mu}\int_\Omega(\vec{b}\cdot\nabla\phi_h)(\vec{b}\cdot\nabla\psi_h)dx = \int_\Omega(\partial_t g_h)\psi_h dx - \frac{1}{\mu}\int_\Omega f_h(\vec{b}\cdot\nabla\phi_h)dx \qquad \forall\psi_h \in V_h^2. \tag{62}$$

To fully discretize the problem also in time, we choose N_t+1 time instants $\{t^n\}_{n=0}^{N_t}$ equispaced with a temporal step size $\Delta t = \frac{T}{N_t}$ and we apply a Newmark discretization scheme. Therefore, let $v_h^n \approx \partial_t\phi_h(t^n)$ and $a_h^n \approx \partial_{tt}\phi_h(t^n)$ be the discrete approximations of the first-order and second-order temporal derivative of the discrete electrostatic potential ϕ_h, respectively. The Newmark scheme gives the following update rules for the quantities ϕ_h^{n+1} and v_h^{n+1}:

$$\begin{cases} \phi_h^{n+1} = \phi_h^n + \Delta t v_h^n + \frac{\Delta t^2}{4}(a_h^n + a_h^{n+1}) \\ v_h^{n+1} = v_h^n + \frac{\Delta t}{2}(a_h^n + a_h^{n+1}) \end{cases} \tag{63}$$

We can derive from the first equation in (63) an update rule for a_h^{n+1}, which reads:

$$a_h^{n+1} = \frac{4}{\Delta t^2}(\phi_h^{n+1} - \phi_h^n) - \frac{4}{\Delta t} v_h^n - a_h^n \tag{64}$$

Lastly, we evaluate the semi-discrete variational problem (62) at the advanced time step t^{n+1}. By approximating the continuous second-order temporal derivative $\partial_{tt}\phi_h(t^{n+1})$ with the discrete acceleration a_h^{n+1} and substituting the kinematic relation (64), we can collect all the unknown terms involving ϕ_h^{n+1} on the left-hand side. This yields the fully discrete algebraic system:

$$\begin{aligned} \frac{4}{\Delta t^2}\int_\Omega \nabla_\perp \phi_h^{n+1} \cdot \nabla_\perp \psi_h \, dx + \frac{1}{\mu}\int_\Omega (\vec{b}\cdot\nabla\phi_h^{n+1})(\vec{b}\cdot\nabla\psi_h)\, dx = \\ \int_\Omega \nabla_\perp \left(\frac{4}{\Delta t^2}\phi_h^n + \frac{4}{\Delta t} v_h^n + a_h^n \right) \cdot \nabla_\perp \psi_h \, dx + \int_\Omega (\partial_t g_h^{n+1})\psi_h \, dx - \frac{1}{\mu}\int_\Omega f_h^{n+1}(\vec{b}\cdot\nabla\psi_h)\, dx \end{aligned} \tag{65}$$

where f_h^{n+1} and $\partial_t g_h^{n+1}$ denote the continuous source terms evaluated at the time instant t^{n+1}. Since the fields ϕ_h^n, v_h^n, and a_h^n are entirely known from the previous time step, this variational formulation defines a standard linear system that can be algebraically inverted to compute the new electrostatic potential ϕ_h^{n+1}. Once ϕ_h^{n+1} is determined, the auxiliary temporal variables a_h^{n+1} and v_h^{n+1} are sequentially updated using equation (64) and the second relation in the Newmark scheme (63), respectively.

Finally, to complete the time-stepping iteration, we must recover the parallel velocity field u_h. Rather than relying on a globally coupled solver, we discretize the first equation of the original strong system, $\partial_t u = \frac{1}{\mu}(\vec{b}\cdot\nabla\phi + f)$, using the unconditionally stable Crank-Nicolson method. Because the electrostatic potential ϕ_h is now fully resolved at both t^n and t^{n+1}, the Crank-Nicolson formulation yields a direct and explicit linear update formula for the parallel velocity:

$$u_h^{n+1} = u_h^n + \frac{\Delta t}{2\mu}\left(\vec{b}\cdot\nabla\phi_h^{n+1} + \vec{b}\cdot\nabla\phi_h^n + f_h^{n+1} + f_h^n \right) \tag{66}$$

This sequential decoupling strategy significantly reduces the computational burden at each time step. Instead of assembling and inverting a large, monolithic block matrix that couples u_h and ϕ_h, Method 2 requires only the inversion of the symmetric positive-definite stiffness matrix associated with (65), followed by a series of explicit algebraic updates for the temporal derivatives and the parallel velocity.

5.2. Test Case 5: Coupled Quadratic FEM for Alfvén Waves - Method 1

The first numerical test case for checking the performance of recovery-based error estimators in the Alfvén wave setting is described here in a simple 2D domain $\Omega = [0, \pi]^2$. Following the same numerical framework as described in [6], the ratio between electron and ion mass is set to unity, namely $\mu = 1.0$, and the normalized magnetic vector field is aligned along the x-direction, which gives $\vec{b}(x, y) = (1.0, 0.0)$. For simplicity, we set also $f = g = 0$. This setting gives an exact analytical solution available, which reads:

$$\phi(x, y, t) = \sin(\omega t)\sin(k_x x)\sin(k_y y) \qquad u(x, y, t) = \frac{k_y}{\sqrt{\mu}}\sin(k_y y)(1 - \cos(k_x x)\cos(\omega t)) \tag{67}$$

where $k_x = 1.0$ and $k_y = 1.0$ denote the wavenumbers governing the shear electrostatic Alfvén wave on both the x- and y- direction, and $\omega = \frac{k_x}{k_y\sqrt{\mu}}$ is the angular frequency.

The spatial domain is discretized using a sequence of progressively refined structured triangular meshes, and the problem is numerically discretized following the coupled Method 1 with Finite Element Method on piecewise quadratic polynomials. To determine the different refinement sizes in space, the baseline mesh size is firstly determined accordingly to the minimum physical wavelength of the system, therefore $h_{\text{base}} = \min(2\pi/k_x, 2\pi/k_y)/20 = \pi/10$. This yields the space refinements to have a mesh size $h \in \{\pi/5, \pi/10, \pi/20, \pi/40\}$. The system is then evolved in time up to a final time instant $T = 0.875 \times (2\pi/\omega) \approx 5.498$, to avoid any trivial symmetry point in the temporal period. To advance the system with Crank-Nicolson, the scheme uses a specific time step scaling, establishing $\Delta t = 0.5\sqrt{\mu}h^2$. This quadratic reduction in the time step is critical for the numerical analysis; indeed, since the Crank-Nicolson method guarantees $\mathcal{O}(\Delta t^2)$ order of convergence, scaling $\Delta t \propto h^2$ mathematically drives the temporal truncation error to $\mathcal{O}(h^4)$. This allows the temporal error to remain subdominant, preventing it from interfering with the measurement of the spatial discretization errors and the analysis of the performance of the recovery-based error estimators.

For the recovery-based error estimation in this test case, we consider both terms of the natural energy norm (52): the L^2-norm of the error for the parallel velocity $u(x, y, t)$ and the L^2-norm of the error for the perpendicular gradient of the electrostatic potential $\phi(x, y, t)$. Just like in the acoustic wave numerical tests, we compute the space-time error using a Root Mean Square (RMS) over the time window $(T - m\Delta t, T]$, considering the last $m = 20$ timeslabs. Based on the numerical implementation, these temporal integrals are computed using the trapezoidal rule.

To estimate the error for the parallel velocity, $\|u(\cdot, T) - u_h(\cdot, T)\|_{L^2(\Omega)}$, we apply the L^2-patch recovery exactly as described in Section 3.9. This provides the enriched solution u_h^*, which allows us to compute the RMS-in-time of the estimator $\|u_h^* - u_h\|_{L^2(\Omega)}$.

For the perpendicular gradient error, $\|\nabla_\perp\phi(\cdot, T) - \nabla_\perp\phi_h(\cdot, T)\|_{L^2(\Omega)}$, we only need the perpendicular projection of the recovered gradient. The standard recovery operator G_h computes the full spatial gradient vector $G_h\phi_h = (G_x, G_y)^T$. To extract just its perpendicular component, we define the projection matrix P:

$$P = I - \vec{b} \otimes \vec{b} \tag{68}$$

where I is the 2×2 identity matrix and $\vec{b} = (1, 0)^T$ is the unit vector parallel to the magnetic field. Multiplying the fully recovered gradient by this matrix gives the perpendicular recovered gradient, denoted as $PG_h\phi_h$.
Finally, we replace the exact perpendicular gradient $\nabla_\perp \phi$ with this recovered quantity. The resulting spatial error indicator is then evaluated by computing the RMS-in-time of $\|PG_h\phi_h - \nabla_\perp \phi_h\|_{L^2(\Omega)}$.

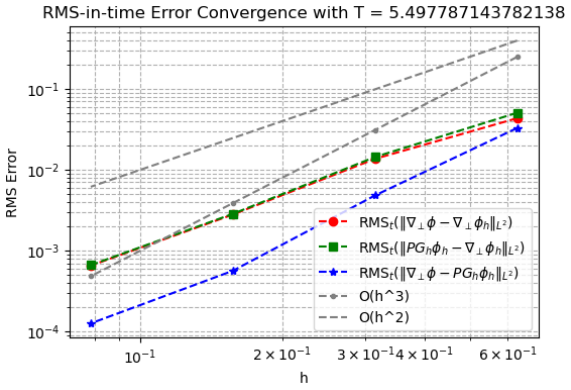

(a) Convergence rates for the error of $\nabla_\perp \phi$ on the 2D Alfvén Wave Equation.

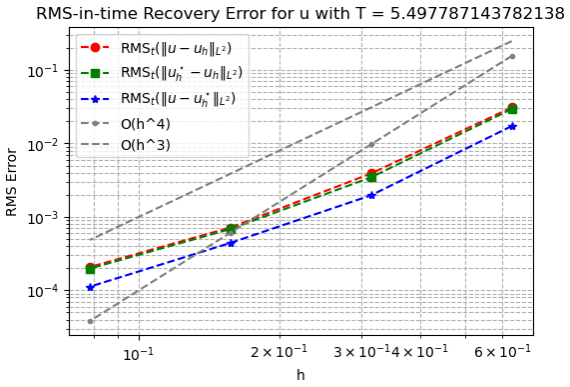

(b) Convergence rates for the error of u on the 2D Alfvén Wave Equation.

Figure 10: Exact errors (red), *a-posteriori* error estimators (green) and superconvergent errors (blue) for the 2D Alfvén Wave Equation solved with Method 1 (Coupled Equation with FEM on $\mathbb{P}^2$.)

Figure 10 shows the convergence rates obtained by the exact errors and the recovery-based error indicators for both the parallel velocity u and the perpendicular gradient of the electrostatic potential $\nabla_\perp \phi$. Even if the plots show asymptotical exactness of both the estimators, the convergence rates clearly detach from theoretical expectations. Indeed, whilst normally for a FEM discretization with piecewise quadratic polynomials we do expect order 2 for the L^2-norm of the gradient of the error, and order 3 for the L^2-norm of the error, one can observe that for finer meshes, the order stabilizes to $\mathcal{O}(h^2)$ for all the quantities (exact errors, *a-posteriori* error indicators and superconvergent quantities) for both the plots.
This order reduction is strictly connected to the stability of the Finite Element Method applied to the coupled problem. Indeed, as recently demonstrated in the theoretical framework described in [6], the standard energy argument restricts the global convergence order to match the lowest-order spatial interpolant present in the formulation. When utilizing continuous finite elements of degree 2 alongside a second-order temporal integrator like Crank-Nicolson, the standard analytical procedure shows a coupled global error bound of the following structural form:

$$\|u - u_h\|_{L^\infty(0,T;L^2(\Omega))} + \|\nabla_\perp(\phi - \phi_h)\|_{L^\infty(0,T;L^2(\Omega))} \leq C(\Delta t^2 + h^2) \tag{69}$$

This joint inequality highlights a distinct theoretical sub-optimality regarding the parallel velocity field u. Because the approximation error of the electrostatic potential ϕ must be measured via its perpendicular gradient in the energy norm, its theoretical spatial convergence is strictly limited to $\mathcal{O}(h^2)$. Through the monolithic nature of the energy estimate, this lower-order gradient error inevitably bounds the entire system. Consequently, the formal mathematical proof can only guarantee an $\mathcal{O}(h^2)$ convergence rate for the L^2-error of u. This estimate is considered strictly suboptimal: an independent projection onto a finite element space V_h^r with piecewise polynomials of degree r theoretically possesses the capacity to achieve an $\mathcal{O}(h^{r+1})$ convergence in the L^2 norm. While numerical experiments often demonstrate that u_h successfully recovers this optimal $\mathcal{O}(h^{r+1})$ scaling, the intrinsic coupling required to mathematically close the energy estimates prevents the standard *a priori* analysis from rigorously capturing this higher-order behavior, masking it behind the dominant error of the potential gradient.

5.3. Test Case 6: Decoupled Quadratic FEM for Alfvén Waves - Method 2

In the second numerical test case, we check the performance of the recovery-based error estimators in the setting of the Alfvén Waves discretized numerically following the decoupled strategy, as defined in Method 2 of Section 5. The numerical setting, together with the exact analytical solution, are the same of Test Case 5 described in Section 5.2.
The most important aspect to mention here is that the natural energy norm for the decoupled problem changes when switching from coupled problem to the decoupled one. To rigorously derive this new energy norm, we consider the homogeneous form of the decoupled equation for the electrostatic potential (61) (i.e. with $f = g = 0$):

$$\partial_{tt}\mathrm{div}(\nabla_\perp \phi) + \frac{1}{\mu}\mathrm{div}(\vec{b}(\vec{b} \cdot \nabla\phi)) = 0 \tag{70}$$

To construct the corresponding energy functional, we multiply the equation by $-\partial_t \phi$ and integrate over the spatial domain Ω:

$$-\int_\Omega \partial_t\phi\,[\nabla_\perp \cdot (\partial_{tt}\nabla_\perp \phi)]\,dx - \frac{1}{\mu}\int_\Omega \partial_t\phi\left[\nabla \cdot (\vec{b}(\vec{b} \cdot \nabla\phi))\right]dx = 0 \tag{71}$$

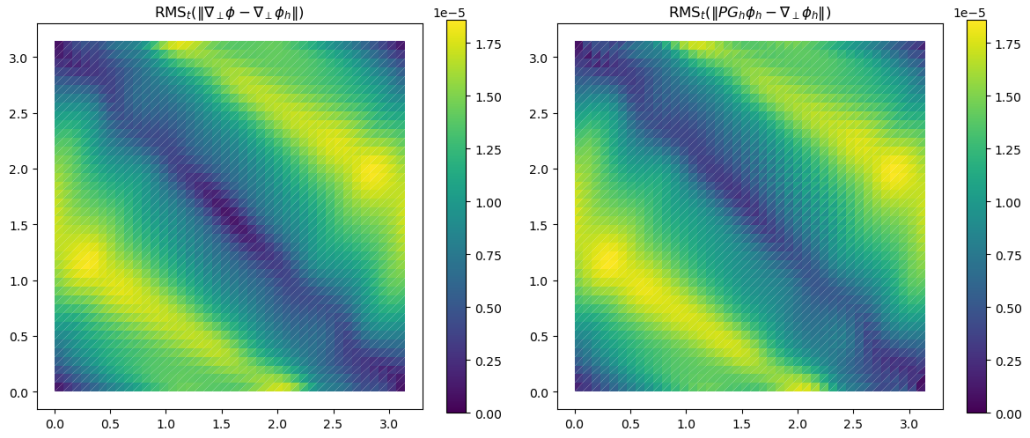

(a) Element-wise distribution of the $\nabla_\perp \phi$ error indicator for the 2D Alfvén Wave Equation solved with Method 1 (Coupled Equation with FEM on $\mathbb{P}^2$): on the left, the RMS-in-time of the exact error; on the right, the RMS-in-time of the recovery-based error indicator.

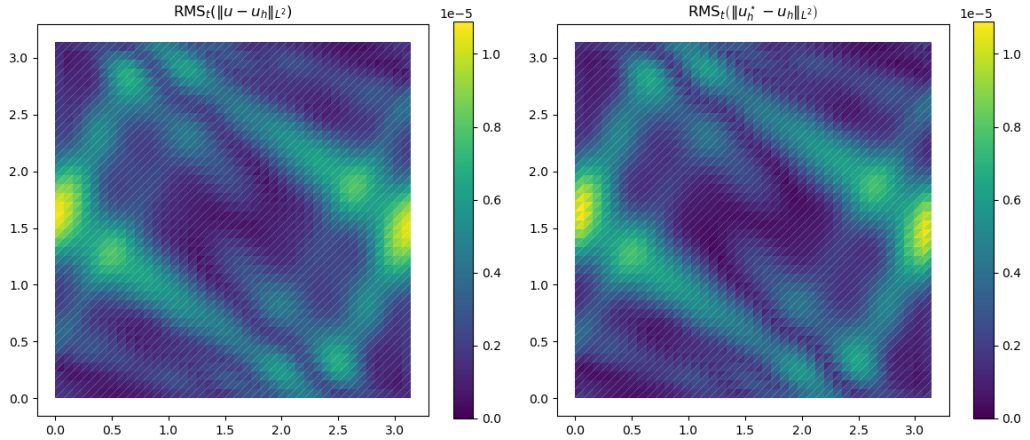

(b) Element-wise distribution of the u error indicator for the 2D Alfvén Wave Equation solved with Method 1 (Coupled Equation with FEM on $\mathbb{P}^2$): on the left, the RMS-in-time of the exact error; on the right, the RMS-in-time of the recovery-based error indicator.

Figure 11: Localized distribution of the recovery-based error indicators for the 2D Alfvén Wave Equation solved with Method 1 (Coupled Equation with FEM on $\mathbb{P}^2$).

We then apply integration by parts to both terms. Assuming homogeneous Dirichlet boundary conditions for φ such that the boundary integrals identically vanish, the equation becomes:

$$\int_\Omega \nabla_\perp(\partial_t\phi)\cdot(\partial_{tt}\nabla_\perp\phi)\,dx + \frac{1}{\mu}\int_\Omega(\vec{b}\cdot\nabla\partial_t\phi)(\vec{b}\cdot\nabla\phi)\,dx = 0 \tag{72}$$

Recognizing that the directional derivative along the magnetic field is $\vec{b}\cdot\nabla = \nabla_\parallel$, we can rewrite the integrands using the chain rule for temporal derivatives:

$$\frac{1}{2}\frac{d}{dt}\int_\Omega |\nabla_\perp\partial_t\phi|^2\,dx + \frac{1}{2\mu}\frac{d}{dt}\int_\Omega |\nabla_\parallel\phi|^2\,dx = 0 \tag{73}$$

This relation implies that the sum of the spatial integrals remains constant over time. Therefore, the natural energy norm for the decoupled formulation, evaluated strictly in terms of the electrostatic potential, is defined as:

$$\|\phi\|^2_{E,\text{decoupled}} = \|\nabla_\perp\partial_t\phi\|^2_{L^2(\Omega)} + \frac{1}{\mu}\|\nabla_\parallel\phi\|^2_{L^2(\Omega)} \tag{74}$$

By recalling the continuous kinematic relation from the original strong system (51), specifically $\partial_t u = \frac{1}{\mu}\nabla_\parallel\phi$, it becomes evident that the second term is physically equivalent to $\mu\|\partial_t u\|^2_{L^2(\Omega)}$. In other words, while the coupled norm in (52) evaluates the magnitude of the physical state (u,ϕ), the decoupled energy norm strictly measures the kinetic variations of the system via the rates of change $(\partial_t u, \partial_t\phi)$.

Evaluating the *a-posteriori* recovery-based error estimators in the context of this new energy norm introduces a specific numerical challenge regarding the spatial continuity of the fields. Within the decoupled numerical framework, the parallel velocity u_h is updated algebraically using the spatial gradient of the electrostatic potential, as done in (66). Because the gradient of a continuous $\mathbb{P}^2$ field is inherently discontinuous across element boundaries, the resulting updated variable u_h naturally resides in a space of broken quadratic polynomials. Standard nodal-based recovery techniques, such as the L^2-patch enrichment, strictly require globally continuous function spaces to construct well-posed local superconvergent patches.

To perform the construction of the recovery-based error estimators for the RMS-in-time of the natural energy norm in (74), we exploit the continuous approximations directly provided by the numerical scheme. For the second term, which requires evaluating the spatial parallel gradient of the electrostatic potential, we apply the recovery technique described in Section 3.2 to the discrete field ϕ_h. The corresponding parallel recovered gradient is then obtained by taking the scalar product between the fully recovered gradient $G_h\phi_h$ and the magnetic field vector $\vec{b}$. Conversely, to evaluate the first term involving the partial time derivative $\partial_t\phi$, we utilize the discrete Newmark velocity v_h^n. Because v_h^n intrinsically belongs to the same continuous $\mathbb{P}^2$ finite element space as ϕ_h, the recovery operator can be safely and seamlessly applied to it. The perpendicular recovered gradient is subsequently extracted by multiplying $G_h v_h^n$ by the projection matrix P, following the identical approach utilized in Method 1. The numerical performance of these estimators is assessed by tracking the RMS-in-time error evolution.

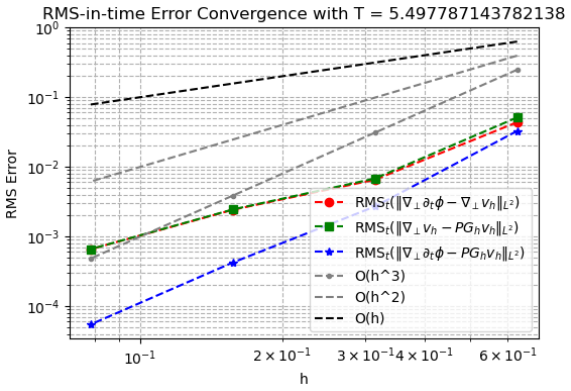

(a) Convergence rates for the RMS error of $\nabla_\perp\partial_t\phi$ on the 2D Alfvén Wave Equation.

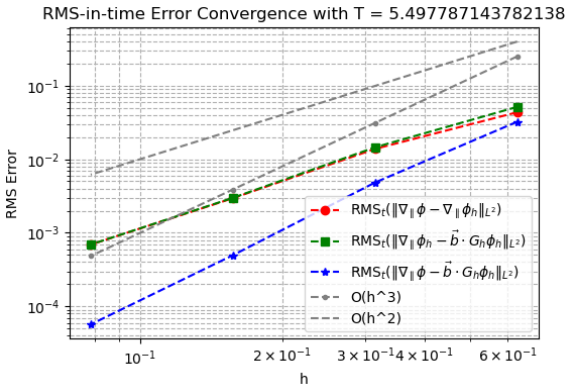

(b) Convergence rates for the RMS error of $\nabla_\parallel\phi$ on the 2D Alfvén Wave Equation.

Figure 12: Exact errors (red), *a-posteriori* error estimators (green) and superconvergent errors (blue) for the natural energy norm of the 2D Alfvén Wave Equation solved with Method 2 (Decoupled Equation with FEM on $\mathbb{P}^2$.)

The associated convergence plots in Figure 12 demonstrate that the recovered quantities accurately approximate the exact spatial errors for both components of the decoupled energy norm. Specifically, the numerical evaluations confirm that the estimators work perfectly, strictly respecting the theoretically expected $\mathcal{O}(h^2)$ order of convergence. This indicates that, when operating on suitable continuous fields, the gradient recovery operators maintain their asymptotic exactness without suffering from the continuity breakdowns that affect the explicitly updated parallel velocity u_h.

Beyond the evaluation of the spatial gradients, this decoupled framework provides the necessary mathematical environment to conclusively validate the L^2-norm recovery technique introduced in Section 3.9. In the previous test case, the

sub-optimal spatial convergence induced by the monolithic mixed formulation fundamentally hindered the recovery of the primal variables. By contrast, isolating the electrostatic potential into an independent wave equation mathematically restores the optimal convergence rates for the primary finite element spaces. Consequently, applying the polynomial enrichment procedure directly to ϕ_h yields a superconvergent proxy solution ϕ_h^*, allowing us to compute the local and global estimators based on the RMS-in-time of the norm $\|\phi_h^* - \phi_h\|_{L^2(\Omega)}$. The numerical convergence plot in Figure 13 shows that this procedure works perfectly, successfully capturing the expected higher-order convergence. This decisively demonstrates that the recovery degradation observed in Section 5.2 was entirely driven by the structural stability limitations of the coupled finite element system, fully accrediting the mathematical robustness of the recovery technique itself when the underlying approximation is stable.

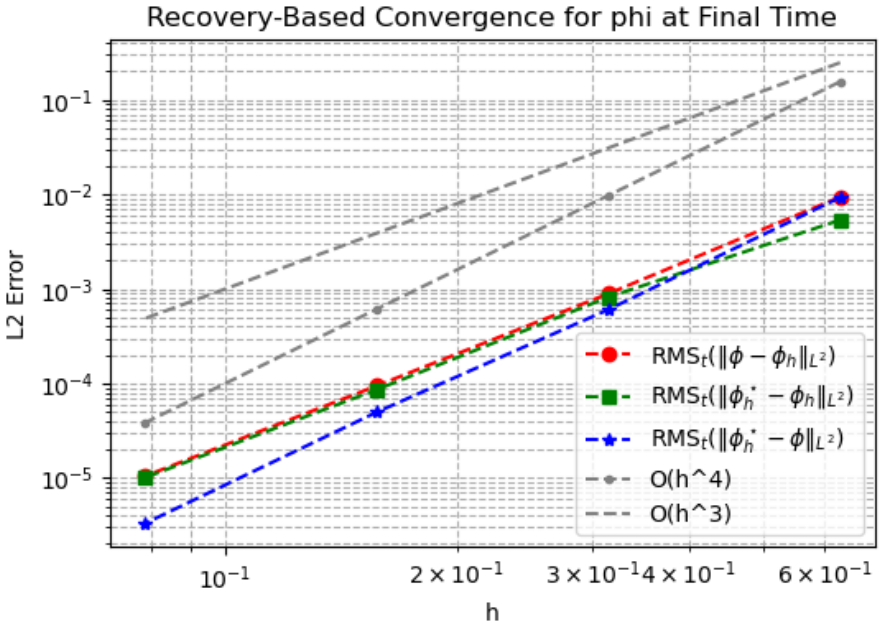

Figure 13: Convergence rates for the exact error, the recovery-based estimator, and the superconvergent proxy of the electrostatic potential in the RMS-in-time L^2-norm ($\mathrm{RMS}_t(\|\phi - \phi_h\|_{L^2(\Omega)})$) for the 2D Alfvén Wave Equation solved with the decoupled Method 2.

Lastly, both the tests done with coupled and decoupled FEM show in Figures 11, 14 that the recovery-based error indicator computed in the energy norm performs well also in localizing the error on each element. Indeed, comparing for each figure the exact error localized on each element (on the left) with the corresponding value of the error indicator, one can clearly observe that the estimation is well performed, due to the asymptotical exactness of the estimator.

5.4. Test Case 7: Adaptive Mesh Refinement (AMR) Strategy on a 2D Anular Domain

We evaluate the practical performance of our a-posteriori estimators through a targeted Adaptive Mesh Refinement (AMR) approach. First, we set up a physically relevant geometry for plasma physics: a mapped annulus domain $\Omega = \{(x, y) \in \mathbb{R}^2 : r_{in}^2 < x^2 + y^2 < r_{out}^2\}$, using an inner radius $r_{in} = 0.35$ and an outer radius $r_{out} = 1.0$. We use an electron-to-ion mass ratio of $\mu = 0.0005$. We initialize the system with zero source terms ($f = g = 0$). To generate a traveling Alfvén wave, the initial parallel velocity in polar coordinates is set to $u_0(r, \theta) = \sin\left(\pi \frac{r - r_{in}}{r_{out} - r_{in}}\right) \sin(m\theta)$ with an azimuthal mode $m = 4.0$. To maintain the correct wave phase, the initial electrostatic potential is strictly tied to the velocity via $\phi_0(r, \theta) = -\sqrt{\mu} u_0(r, \theta)$.
Instead of modifying the grid at every single time step, the decoupled numerical scheme is advanced on a fixed, structured triangular mesh. For the spatial discretization, we rely on piecewise quadratic ($\mathbb{P}^2$) finite elements with spatial discretization parameter $h = 0.125$. The temporal integration handles the electrostatic potential ϕ via a damped Newmark-beta scheme ($\gamma = 0.6$, $\beta = 0.3025$) to filter out high-frequency oscillations, while the parallel velocity u is advanced explicitly using the Crank-Nicolson method. We link the time step directly to the spatial grid size using the relation $\Delta t = 0.5\sqrt{\mu} h^2$. The solver operates continuously on this baseline grid up to the penultimate time instant, $t = T - \Delta t$ (with the final time set as $T = 0.875 \times (2\pi r_{out}\sqrt{\mu})/m$). As the simulation progresses, we build an error footprint by computing the Root Mean Square (RMS) of the local error indicator, specifically evaluating this over a trailing window of the last $m = 20$ timeslabs. Once we reach $T - \Delta t$, this accumulated RMS error is used to trigger and guide the mesh refinement. After generating the refined grid, the entire kinematic state is projected onto the new mesh through a non-matching interpolation. Finally, the simulation performs one last time step on the newly adapted grid to hit the final time T.
The mesh adaptation is driven strictly by the spatial component of the error indicator. We evaluate the RMS in time of

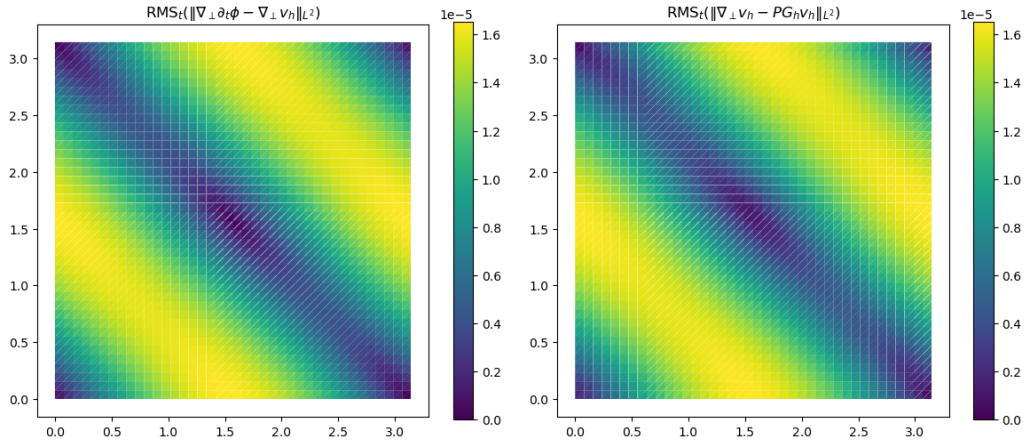

(a) Element-wise distribution of the $\nabla_\perp \partial_t \phi$ error indicator for the 2D Alfvén Wave Equation solved with Method 2 (Decoupled Equation with FEM on $\mathbb{P}^2$): on the left, the RMS-in-time of the exact error; on the right, the RMS-in-time of the recovery-based error indicator.

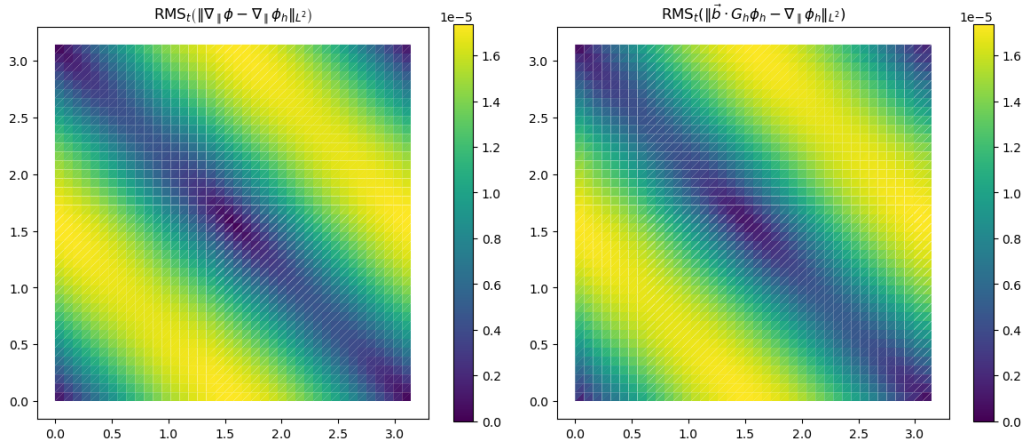

(b) Element-wise distribution of the $\nabla_\parallel \phi$ error indicator for the 2D Alfvén Wave Equation solved with Method 2 (Decoupled Equation with FEM on $\mathbb{P}^2$): on the left, the RMS-in-time of the exact error; on the right, the RMS-in-time of the recovery-based error indicator.

Figure 14: Localized distribution of the recovery-based error indicators for the 2D Alfvén Wave Equation solved with Method 2 (Decoupled Equation with FEM on $\mathbb{P}^2$).

the parallel gradient of the electrostatic potential:

$$\eta_{spatial} = \mathrm{RMS}_t \left(\frac{1}{\sqrt{\mu}} \|\vec{b} \cdot G_h \phi_h - \nabla_{\parallel} \phi_h\|_{L^2(K)} \right)$$

We exclude the temporal error component from the marking logic. Since our numerical setup enforces the scaling $\Delta t \propto h^2$ to guarantee that the temporal truncation error remains subdominant, the time step is intrinsically restrictive. Consequently, refining the mesh based exclusively on the spatial elliptic indicator is a stable and sufficient method to track the steep wave fronts. For the marking procedure, a cell K is marked for refinement if its local error $\eta_{spatial}$ is greater than or equal to 60% of the maximum error registered across the entire domain.
The effectiveness of this procedure is illustrated in Figure 15. As observed in the plots, the highest error concentration occurs close to the inner boundaries of the domain, which is a direct consequence of the complex reflection and propagation dynamics of the Alfvén waves. The left panel displays the localized error distribution for the standard baseline execution without AMR. The right panel shows the outcome of the single-step rewind strategy: the adaptive algorithm successfully detects these critical boundary regions and refines the computational grid precisely where the 60% threshold is triggered. This targeted adaptation not only resolves the sharp gradients locally but also effectively reduces the overall magnitude of the error. Quantitatively, the baseline execution on the original grid (1,664 degrees of freedom) produces a global L^2-norm error of 1.1167×10^{-1}. After applying the AMR procedure, the adapted mesh expands to 2,528 degrees of freedom, which successfully drives the global error down to 9.8661×10^{-2}.

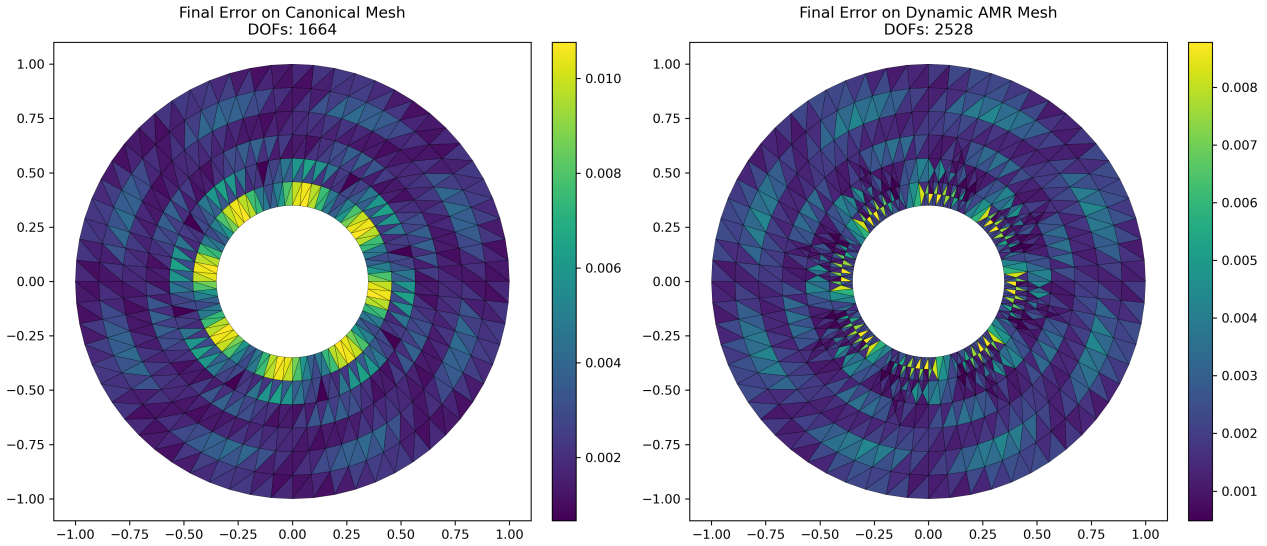

Figure 15: Comparison of the localized error distribution for the Alfvén Wave Equation without Adaptive Mesh Refinement (left) and with the single-step rewind AMR strategy (right) applied at $t = T - \Delta t$.

Conclusions

In this work, our objective was to rigorously analyze both spatial and temporal recovery-based error indicators for hyperbolic problems. The foundation of the model relies on a standard Galerkin finite element method using piecewise linear and quadratic polynomials, paired with Crank-Nicolson and Newmark time-stepping schemes. From there, we applied polynomial preserving recovery techniques to estimate spatial gradients, L^2-norms and temporal derivatives for both acoustic waves and Alfvén waves, according to their respective energy norms. Numerical tests were performed for both the cases, showing that, for the acoustic wave equation, the recovery operators worked exactly as intended, providing accurate error indicators for both space and time. However, applying them to the more complex shear electrostatic Alfvén waves exposed a limitation. The standard coupled formulation caused a loss of spatial stability, which capped the convergence rate and prevented the recovery process from working. We solved this by decoupling the equations, which restored the optimal convergence rates and allowed the estimators to properly measure the system's true energy norm. Finally, we tested the practical use of these estimators by plugging them into an Adaptive Mesh Refinement (AMR) algorithm. The recovered errors successfully tracked the moving wave fronts and refined the mesh only where necessary, close to the inner boundaries where sharp localized gradients arise.
Therefore, recovery-based error estimators are effective also in the case of hyperbolic differential problems, as numerical tests showed both asymptotical exactness of the error indicators with respect to the exact error, and convergence rates which matched with theoretical expectations, achieving the superconvergence property. On the other hand, recovery-based error techniques rely strongly on the superconvergence property, which can be obtained under strong assumptions made on the regularity of the exact solution and supercloseness properties of the numerical methods used in the discretization. When the physical solution exhibits steep layers and sharp gradients, the recovery-based post-processing

operators struggle to create a more accurate version of the gradients, unless the mesh size is highly refined. Furthermore, in the context of plasma physics, current scientific work has already extended the numerical simulations of shear electrostatic Alfvén waves to a 3D setting. Therefore, the 2D Alfvén model represents a highly idealized physical state. Regarding future developments, the most straightforward next step would be moving this analysis into fully 3D toroidal domains. This is basically required in order to simulate realistic magnetic confinement devices. Recently, there have been efforts to simulate turbulent plasma dynamics in full 3D *tokamak* geometries, though these are currently limited to Finite Difference methods. A natural future development would be to either adapt the recovery-based estimators for Finite Differences described in [25] to these specific settings, or to discretize the 3D plasma models using the Finite Element Method so our proposed estimators can be directly applied. Lastly, since the shear Alfvén wave model is just a fast sub-system, a final long-term goal would be to apply this decoupled, *a-posteriori* recovery-based error strategy to the complete, nonlinear drift-reduced Braginskii equations to model full macroscopic plasma turbulence.

References

[1] Assyr Abdulle and Gilles Vilmart. The effect of numerical integration in the finite element method for nonmonotone nonlinear elliptic problems with application to numerical homogenization methods. *Comptes Rendus Mathematique*, 349(19–20):1041–1046, 2011.

[2] Mark Ainsworth and J. Tinsley Oden. A posteriori error estimation in finite element analysis. *Computer Methods in Applied Mechanics and Engineering*, 142(1–2):1–88, 1997.

[3] Martin S. Alnæs, Anders Logg, Kristian B. Ølgaard, Marie E. Rognes, and Garth N. Wells. Unified form language: A domain-specific language for weak formulations of partial differential equations. *arXiv preprint arXiv:1211.4047*, 2012.

[4] Garth A. Baker. Error estimates for finite element methods for second order hyperbolic equations. *SIAM Journal on Numerical Analysis*, 13(4):564–576, 1976.

[5] Klaus-Jürgen Bathe. Finite element method. *Wiley encyclopedia of computer science and engineering*, pages 1–12, 2007.

[6] Annalisa Buffa, Timon Miehling, Marco Picasso, and Markus Renoldner. Well-posedness and finite element approximation of the electrostatic shear alfvén wave equations, 2026.

[7] Carsten Carstensen. Some remarks on the history and future of averaging techniques in a posteriori finite element error analysis. *ZAMM – Journal of Applied Mathematics and Mechanics / Zeitschrift für Angewandte Mathematik und Mechanik*, 84(1):3–21, 2004.

[8] Philippe G. Ciarlet. *The Finite Element Method for Elliptic Problems*, volume 4 of *Studies in Mathematics and its Applications*. North-Holland, Amsterdam, 1978.

[9] Gary Cohen. *Higher-Order Numerical Methods for Transient Wave Equations*. Springer, 2003.

[10] J. S. Dokken, I. A. Baratta, J. P. Dean, M. Habera, J. S. Hale, C. Richardson, M. E. Rognes, N. Sime, and G. N. Wells. DOLFINx: The next generation FEniCS problem solving environment, December 2023.

[11] Georges Duvaut and Jacques-Louis Lions. *Inequalities in mechanics and physics*. Springer-Verlag, Berlin, New York, 1976.

[12] Jeffrey P. Freidberg. *Ideal MHD*. Cambridge University Press, 2014.

[13] Robert J. Goldston and Paul H. Rutherford. *Introduction to Plasmas and Controlled Fusion*. CRC Press, 1995.

[14] Olga Gorynina, Alexei Lozinski, and Marco Picasso. An easily computable error estimator in space and time for the wave equation, 2017.

[15] Olga Gorynina, Alexei Lozinski, and Marco Picasso. An easily computable error estimator in space and time for the wave equation. *ESAIM: Mathematical Modelling and Numerical Analysis*, 53(3):729–747, 2019.

[16] Thomas Grätsch and Klaus-Jürgen Bathe. A posteriori error estimation techniques in practical finite element analysis. *Computers & Structures*, 83(4–5):235–265, 2005. HAL Id: hal-01390203.

[17] Richard D. Hazeltine and James D. Meiss. *Plasma Confinement*. Courier Corporation, 2003.

[18] Qun Lin, Hehu Xie, and Jinchao Xu. Lower bounds of the discretization error for piecewise polynomials. *Mathematics of Computation*, 83(285):1–13, 2014.

[19] Ahmed Naga and Zhimin Zhang. A posteriori error estimates based on the polynomial preserving recovery. *SIAM Journal on Numerical Analysis*, 42(4):1780–1800, 2004.

[20] Marco Picasso. Numerical study of an anisotropic error estimator in the $l^2(h^1)$ norm for the finite element discretization of the wave equation. *SIAM Journal on Scientific Computing*, 32(4):2213–2234, 2010.

[21] Alfio Quarteroni and Alberto Valli. *Numerical Approximation of Partial Differential Equations*, volume 23 of *Springer Series in Computational Mathematics*. Springer Berlin, Heidelberg, 1994.

[22] Pierre-Arnaud Raviart and Jean-Marie Thomas. *Introduction à l'analyse numérique des équations aux dérivées partielles*. Masson, Paris, 1983.

[23] P. Ricci, F. D. Halpern, S. Jolliet, J. Loizu, A. Mosetto, A. Fasoli, I. Furno, and C. Theiler. Simulation of plasma turbulence in scrape-off layer conditions: the GBS code, simulation results and code validation. *Plasma Physics and Controlled Fusion*, 54(12):124047, 2012.

[24] Micol Rochery, Yaman Güçlü, Martin L. L. Michel, and Eric Sonnendrücker. Conservative semi-lagrangian schemes for the electrostatic shear Alfvén wave equations. *Journal of Computational Physics*, 2024.

[25] Ferhat Sindy, Annalisa Buffa, and Marco Picasso. A recovery-based error indicator for finite difference methods, 2026.

[26] Nils-Erik Wiberg and X. D. Li. Superconvergent patch recovery of finite element solution and a posteriori error L^2 norm estimate. *Communications in Numerical Methods in Engineering*, 10(4):313–320, 1994.

[27] Jinchao Xu and Zhimin Zhang. Analysis of recovery type a posteriori error estimators for mildly structured grids. *Mathematics of Computation*, 73(247):1139–1152, 2004.

[28] A. Zeiler, J. F. Drake, and B. Rogers. Nonlinear reduced braginskii equations with ion thermal dynamics in toroidal plasma. *Physics of Plasmas*, 4(6):2134–2138, 1997.

[29] Zhimin Zhang and Ahmed Naga. A new finite element gradient recovery method: Superconvergence property. *SIAM Journal on Scientific Computing*, 26(4):1192–1213, 2005.

[30] O. C. Zienkiewicz and J. Z. Zhu. The superconvergent patch recovery and a posteriori error estimates. part 1: The recovery technique. *International Journal for Numerical Methods in Engineering*, 33(7):1331–1364, 1992.

[31] O. C. Zienkiewicz and J. Z. Zhu. The superconvergent patch recovery (spr) and adaptive finite element refinement. *Computer Methods in Applied Mechanics and Engineering*, 101(1–3):207–224, 1992.

Abstract in lingua italiana

Questo studio adatta le tecniche di stima dell'errore recovery-based, tradizionalmente impiegate per i problemi ellittici, alle equazioni d'onda iperboliche. Il modello matematico si avvale di un metodo standard agli elementi finiti di Galerkin, utilizzando polinomi lineari o quadratici a tratti. Tale discretizzazione spaziale è associata agli schemi di integrazione temporale di Crank-Nicolson e Newmark. Per stimare i gradienti spaziali, le norme in L^2 e le derivate temporali, vengono applicate tecniche di polynomial preserving recovery, in accordo con la norma naturale dell'energia del problema. Nel caso base dell'equazione delle onde acustiche, le quantità recuperate riescono a catturare con precisione sia l'errore spaziale che quello temporale, mantenendo i tassi di convergenza asintotica attesi. Tuttavia, l'estensione di questo approccio alle onde di Alfvén di taglio (shear Alfvén waves) evidenzia un problema strutturale. La formulazione mista limita artificialmente la convergenza spaziale, a causa di un vincolo di stabilità che fa inevitabilmente fallire gli operatori di recupero. Passando a uno schema disaccoppiato, è possibile aggirare efficacemente questo ostacolo legato alla stabilità. Questo passaggio ripristina l'ordine di convergenza ottimale per i campi primari e permette agli stimatori a posteriori di approssimare accuratamente l'effettiva norma dell'energia disaccoppiata del sistema.

Parole chiave: stima dell'errore basata sul recupero; convergenza a posteriori; equazioni differenziali iperboliche; metodo agli elementi finiti; schemi di integrazione temporale; raffinamento adattivo di mesh

Acknowledgements

I would like to express my deepest gratitude to Pablo and Prof. Buffa for allowing me to conclude my academic journey within the MNS Department here at EPFL. It has been amazing to experience the daily life of PhD students and PostDocs firsthand, and having the chance to work on my project with so many daily interactions provided the perfect motivation to finish my studies on a high note. I would also like to thank everyone in the MNS department, especially my two colleagues, Davor and Yannis, for patiently answering all my questions and for your genuine availability. A special thank you goes to my Polimi advisor, Prof. Antonietti, who has been a true guide throughout my entire Master's degree, right from the start when I was still unsure about what to do after my Bachelor's. The humanity and professionalism she demonstrated beyond the lectures have been truly inspiring, encouraging me to persevere through this invaluable experience. Last but not least, my most important "thank you" goes to my true guide over these past four months: Ferhat. Thank you for your daily support and help, even when I was bothering you for the eighth time in a single day. Starting from the semester project, the collaborative atmosphere you created allowed me to truly work at my best. Hard work was certainly required for these two projects, but collaborating with you added immense value to this entire experience. I genuinely hope that our paths can cross again in the future.
To my family, especially my mom and my dad, your constant presence even from abroad has been the right engine to continue this path. Difficulties have been a constant presence, but your support and your patience in being actively present for me made me continue my path up to the end. I am grateful and I will never stop being thankful to you.
To all the friends I made here in Lausanne, particularly Francesco, Riccardo, Leonardo, Emilia and Maddalena, I am grateful to have shared these two fantastic years with you all. We shared moments of joy, fun, emotions, sport, anxiety, difficulty, laughters, in such a powerful way that I will never forget. I am going to miss all of these moments, but I am extremely grateful for having been my true support during my moments of ups and downs.
We do never know the true value of a moment until it becomes a memory, that's why I know for sure that this amazing experience will never be forgotten, and it will always have a special place in my memories.